

Modeling and Simulation of Plasma-Assisted Vertically-aligned Carbon Nanotubes Array Based Solar Cells

MASTER OF SCIENCE

**in
Physics**

By

KULDEEP SINGH
(2K23/MSCPHY/27)

&

RONIT SHRIVASTAVA
(2K23/MSCPHY/70)

Under the supervision of

Prof. Suresh C. Sharma
Department of Applied Physics
Delhi Technological University

Department of Applied Physics



DELHI TECHNOLOGICAL UNIVERSITY
(Formerly Delhi College of Engineering)
Shahbad Daultpur, Main Bawana Road, Delhi – 110042.

June 2025



DELHI TECHNOLOGICAL UNIVERSITY

(Formerly Delhi College of Engineering)

Shahbad Daulatpur, Main Bawana Road, Delhi - 110042

CANDIDATE'S DECLARATION

We, **KULDEEP SINGH** (Roll No. 2K23/MSCPHY/27) and **RONIT SHRIVASTAVA** (Roll No. 2K23/MSCPHY/70), students of M.Sc. Physics, hereby declare that the work presented in the dissertation titled “*Modeling and Simulation of Plasma-Assisted Vertically-aligned Carbon Nanotubes Array Based Solar Cells*” submitted in partial fulfilment of the requirements for the award of the Master of Science degree, is an original and authentic record of our work. This research was conducted from September 2024 to May 2025 under the guidance of **Prof. Suresh C. Sharma**, Department of Applied Physics, Delhi Technological University, Delhi.

The content presented in this thesis has not been submitted by us for the award of any other degree, either at this or any other institution.

Place: Delhi

Date: 09/06/2025

Candidate's Signature

Kuldeep Singh
1. Kuldeep Singh

Rt
2. Ronit Shrivastava

This is to certify that the student has made all the corrections suggested by the examiner in the thesis, and the statement made by the candidate is accurate to the best of our knowledge.

S Sharma
06.06.2025
Signature of Supervisor

Prof. Suresh C. Sharma

**Department of Applied Physics
Delhi Technological University**



DEPARTMENT OF APPLIED PHYSICS


DELHI TECHNOLOGICAL UNIVERSITY

(Formerly Delhi College of Engineering)
Bawana road, Delhi – 110042

CERTIFICATE

I, hereby certify that the Project Report titled "*Modeling and Simulation of Plasma-Assisted Vertically-aligned Carbon Nanotubes Array Based Solar Cells*" Which is submitted by **RONIT SHRIVASTAVA, Roll No 2K23/MSCPHY/70** and **KULDEEP SINGH, Roll No 2K23/MSCPHY/27**, from the Department of Applied Physics, Delhi Technological University, Delhi, is in partial fulfillment of the requirements for the award of the degree of Master of Science. This report represents the project work conducted by the students under my supervision. To the best of my knowledge, this work has not been submitted, in whole or in part, for any degree or diploma at this university or elsewhere.

Place: Delhi Date:09/06/2025


06.06.2025
SUPERVISOR

Prof. Suresh C. Sharma
Department of Applied Physics
Delhi Technological University



DEPARTMENT OF APPLIE PHYSICS

DELHI TECHNOLOGICAL UNIVERSITY

(Formerly Delhi College of Engineering)

Bawana road, Delhi – 110042

ACKNOWLEDGEMENT

We would like to express our deepest gratitude to our project supervisor, **Prof. SURESH C. SHARMA**, for his exceptional guidance, unwavering support, and constant encouragement throughout my academic journey. His insightful teachings and thoughtful advice have been instrumental in shaping my understanding of the subject. I am also deeply thankful to Delhi Technological University for providing an enriching academic environment that fostered my growth and development. The resources, opportunities, and collaborative atmosphere at the university have played a significant role in helping me achieve my goals. I truly appreciate the support of both my professor and my college in making this journey a rewarding one.

Place: Delhi

Date: 09/06/2025

RONIT SHRIVASTAVA

KULDEEP SINGH

ABSTRACT

Our work investigates the use of Carbon Nanotube (CNT) arrays with varying radii and lengths, synthesized via the Plasma-Enhanced Chemical Vapor Deposition (PECVD) method, as absorber layers in solar cells. CNTs with different geometric properties were systematically analyzed to evaluate their impact on the photovoltaic performance of solar cells. The PECVD technique was employed to grow high-quality, well-aligned CNT arrays, with radii and lengths precisely controlled. The effects of CNT radius and length on key solar cell parameters, such as current density, open-circuit voltage, fill factor, and overall efficiency, were simulated using the SCAPS 1D software. Simulation results revealed that both CNT radius and length significantly influenced the performance of the solar cells, with optimal CNT dimensions leading to improved efficiency. The study highlights the potential of tailoring CNT array properties to enhance the performance of solar cells, providing insights into how variations in CNT geometry can be leveraged to optimize the absorber layer in photovoltaic devices.

TABLE OF CONTENTS

Candidate Declaration.....	i
Certificate.....	ii
Acknowledgement.....	iii
Abstract.....	iv
Table Contents	v
List of tables.....	vii
List of figures.....	viii
Abbreviations	x

CHAPTER 1: INTRODUCTION.....1

- 1.1 Solar cell Introduction
- 1.2 Carbon Nanotube Based Solar Cell
- 1.3 Growth of Carbon Nanotubes using Plasma
- 1.4 Application of CNT based Solar cells
- 1.5 Advantages of CNT Based Solar cell
- 1.6 Disadvantages of CNT Based Solar cell
- 1.7 SCAPS Software

CHAPTER 2: MODELING AND SIMULATION OF PLASMA ASSISTED ARRAY OF CNT BASED SOLAR CELL.....10

- 2.1 Introduction Literature Review
- 2.2 Introduction
- 2.3 Solar Cell Structure and (SCAPS Simulation)

CHAPTER 3: CNT SYNTHESIS VIA PECVD.....16

- 3.1 Sub-1 nm VACNT Synthesis via PECVD

CHAPTER 4: SIMULATION WORK.....20

- 4.1 Simulation of Solar Cell parameters in SCAPS-1D
- 4.2 Theoretical Framework for Efficiency CNT-Based Solar Cells
- 4.3 Analytical Modeling Results:

CHAPTER 5: RESULTS AND DISCUSSIONS.....	25
5.1 Effect of Plasma Parameters on the Structural Characteristics of VACNTs	
5.2 Solar Cell characteristics Simulation Results	
5.3 Comprehensive Analysis of Results	
 CHAPTER 6: CONCLUSION AND FUTURE SCOPE	 42
6.1 Future Scope	
 REFERENCES.....	 43
 PLAGIARISM REPORT.....	 51

LIST OF TABLES

S.N	Table No.	Description	Page No.
1	2.1	Simulation values of the proposed Solar cell layers for SCAPS-1D software	15
2	2.2	Proposed Solar cell of SCAPS-1D software Metal contacts parameters	15
3	2.3	Defect in Solar cell layers	15
4	3.1	Variation in Plasma Parameters with Channel Radius	17
5	3.2	Variation in Plasma Parameters with Channel Length	17
6	3.3	Summary table	19
7	4.1	SCAPS-1D Simulation results for ITO/CDS/CNT based solar cell (at constant R)	20
8	4.2	SCAPS-1D Simulation results for ITO/CDS/CNT based solar cell (at constant L)	21
9	4.3	Result from Simulated and Analytical work at constant Length of CNT	23
10	4.4	Result from Simulated and Analytical work at constant Radius of CNT	24
11	5.1	Efficiency Comparison of Solar Cells with Varying CNT dimensions: Simulation, Analytical, and Error Data	40

LIST OF FIGURES

CHAPTER 1:

S.N	Figure No.	Description	Page No.
1	1.1	Schematic Diagram of Solar Cell	1
2	1.2	Different Types of CNTs	4
3	1.3	CNT implement in single solar cell	5
4	1.4	Schematic Diagram of PECVD Machine	7
5	1.5	Interface of SCAPS Software	9

CHAPTER 2:

S.N	Figure No.	Description	Page No.
1	2.1	Schematic Diagram of Solar Cell	12
2	2.2	Solar Cell constructed in SCAPS-1D Software	13

CHAPTER 5

S.N	Figure No.	Description	Page No.
1	5.1	Electron Density Vs CNT Length	25
2	5.2	Ion Density Vs CNT Length	25
3	5.3	Electron Temperature Vs CNT Length	28
4	5.4	Ion Temperature Vs CNT Length	28
5	5.5	Electron Density Vs CNT Radius	30
6	5.6	Ion Density Vs CNT Radius	30
7	5.7	Electron Temperature Vs CNT Radius	32

S.N	Figure No.	Description	Page No.
8	5.8	Ion Temperature Vs CNT Radius	32
9	5.9	Bandgap (eV) VS Thickness of Solar Cell	34
10	5.10	Quantum Efficiency Vs Wavelength graph at constant R	36
11	5.11	Current density Vs Voltage graph at constant R	36
12	5.12	Quantum Efficiency Vs Wavelength graph at constant L	38
13	5.13	Current density Vs Voltage graph at constant L	38
14	5.14	Efficiency Comparison graph	40
15	5.15	Comparing Efficiencies of Present work, Simulated work and Experimental Result	40

ABBREVIATIONS

Table 1 Parameters and Symbols used in the present work

Parameters	Symbols
Effective area of the Solar cell	A
Resistances in series	R _s
Surface recombination velocity for electrons	Se
Electron concentration	N
Current density	J
Recombination rate of Holes	R _p
Ideality factor	n _o
Resistances in Parallel	R _{sh}
Reverse Saturation Current density	J _o
Carbon Nanotubes	CNTs
Recombination rate of Electrons	R _n
Length of CNT	L
Radius of CNT	R
Power Conversion Efficiency	PCE
Electron Temperature	T _{eo}
Ion Temperature	T _{io}
Debye length	λ _D
Solar irradiance	P _{in}
Generation rate of Electrons	G _n
Absolute temperature	T
Electronic charge	q
Electron Density	n _{eo}
Surface recombination velocity for holes	Sh
Ion Density	n _{io}
No. of Carbon Nanotubes (CNTs)	N
Efficiency of Solar cell	η
Power Output	P _{out}
Indium tin oxide	ITO
Open circuit voltage	V _{oc}
Electron current density	J _n
Generation rate of Holes	G _p
Air mass spectrum	AM
Photocurrent density	J _{sc}
Conduction band	CB
Boltzmann's constant	K _B
Valance band	VB
Hole concentration	p
Metal work function	φ
Transparent conductive oxide	TCO
Hole current density	J _p
Quantum efficiency	QE
Surface Potential	V _s
Thickness of Absorber layer	t
Fill factor	FF

CHAPTER 1

INTRODUCTION

1.1 Solar Cell Introduction

Solar cells, or photovoltaic cells, transform sunlight into electrical current using the photovoltaic process [1]. In this process electric current is generated when specific materials are exposed to light [2],[3].

1.1.1 Principle of Solar Cell

This process in solar cell is based on the concept, which is somewhat similar to the photoelectric effect [2]. In the photovoltaic effect, when light strikes a semiconductor material, bound electrons gain sufficient energy to transition to the conduction band, becoming mobile charge carriers [4]. Conversely, in the photoelectric effect, photons eject electrons entirely from a metal surface into vacuum [5]. This distinction—internal charge mobilization versus external electron emission—defines the core principle of photovoltaic energy conversion [1].

1.1.2 Construction of Solar Cell

A solar cell consists of a P-N junction diode, where the N region is very thin (0.3 micrometers) and the P region is much thicker (300 micrometers) [1]. The N region is kept thin to ensure that light can reach the junction without significant absorption [6]. Metallic fingers are deposited on the top of the silicon layer, forming the front contact [7], while the bottom of the P-type silicon layer is coated with a metal (copper), known as the back contact [8].

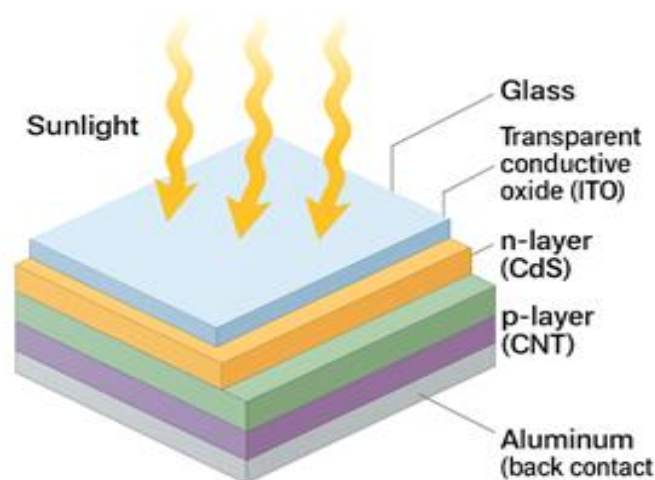


Fig. 1.1 Schematic Diagram of Solar Cell

1.1.3 Working of Solar cell

The photovoltaic effect can be explained as follows: When certain materials, primarily semiconductors like silicon, are exposed to light, photons strike the material's surface. The energy from these photons is absorbed by the electrons, exciting them and causing them to move to a higher energy state [4]. This absorption creates electron-hole pairs, with the electron moving to the conduction band, leaving behind positively charged holes in the valence band [6]. Inside the semiconductor, an internal electric field is created that helps separate these electron-hole pairs [1]. This field drives the excited electrons toward the electron collector electrode (typically the n-type semiconductor) and the holes toward the hole-collecting electrode (typically the p-type semiconductor) [7]. The movement of electrons and holes generates an electric current [9].

1.1.4 Efficiency Calculation for solar cell

The Photo Current Density of semiconducting device i.e. Solar Cell given by

$$J_{sc} = q \int QE(E)b_s(E)dE,$$

Where, q = Charge on electron can be denoted by e also have value $1.6 \times 10^{-19} \text{C}$

$b_s(E)$ = Flux Density of Incident Photons

$QE(E)$ = Probability of incident light particles with energy E which is given to the electron to the Load Circuit [1].

A dark current also found in solar cells denoted by $J_{\text{dark}}(V)$ at an external voltage (V) can be calculated by:

$$J_{\text{dark}}(V) = J_0(e^{qV/nk_B T} - 1),$$

Where, J_0 = constant

N = Ideality factor

K_b = Boltzmann constant

T = Absolute temperature in kelvin

Now, Net current density is equal to the addition of photocurrent density and dark current density. And dark current having same direction. So net current density will be [1],[4]:

$$J = J_0 \left(e^{qV/nk_B T} - 1 \right) - J_{sc}$$

When circuit is open, $J_{dark}(V) = J_{sc}$. Equation for open circuit voltage (V_{oc}) will be [10],[1]:

$$V_{oc} = \frac{kT}{q} \ln \left(\frac{J_{sc}}{J_0} + 1 \right).$$

In a real solar cell, the presence of material resistance, resistance at contact terminals, and leakage current all contribute to energy loss. These resistances can be modelled as two parasitic resistances: series resistance (R_s) and shunt resistance (R_{sh}). The series resistance (R_s) represents the resistances in the current path, such as the contact resistance and internal material resistance, while the shunt resistance (R_{sh}) accounts for leakage current through paths that bypass the junction [7],[11].

The total current density (J) in the solar cell, taking these resistances into account, can be expressed as:

$$J = J_0 \left(e^{q(V-JAR_s)/nk_B T} - 1 \right) + \frac{V - JAR_s}{AR_{sh}} - J_{sc}$$

Where,

A = Solar Cell Effective Area [6],[12].

Definition of Fill Factor (FF):

The Fill factor is explained like it is division of product of $J_m.V_m$ and $J_{sc}.V_{oc}$ respectively [12],[1]:

$$FF = \frac{J_m V_m}{J_{sc} V_{oc}}.$$

Solar cell efficiency (η) with incident light power density (P_{in}) [13],[9]:

$$\eta = \frac{FF \times V_{oc} \times J_{sc}}{P_{in}} \times 100$$

1.2 Carbon nanotube (CNT)

Carbon nanotubes (CNTs) were discovered in 1991 by Japanese scientist Sumio Iijima [14]. CNTs are excellent conductors of electricity but are highly flammable due to their carbon content [15]. Classification of CNTs based on chirality includes single-wall carbon nanotubes (SWCNTs) and multi-wall carbon nanotubes (MWCNTs) [16]. CNTs are formed by folding a graphene sheet: folding a single sheet of graphene cylindrically results in a single-wall CNT, while folding multiple graphene sheets creates a multi-wall CNT [17].

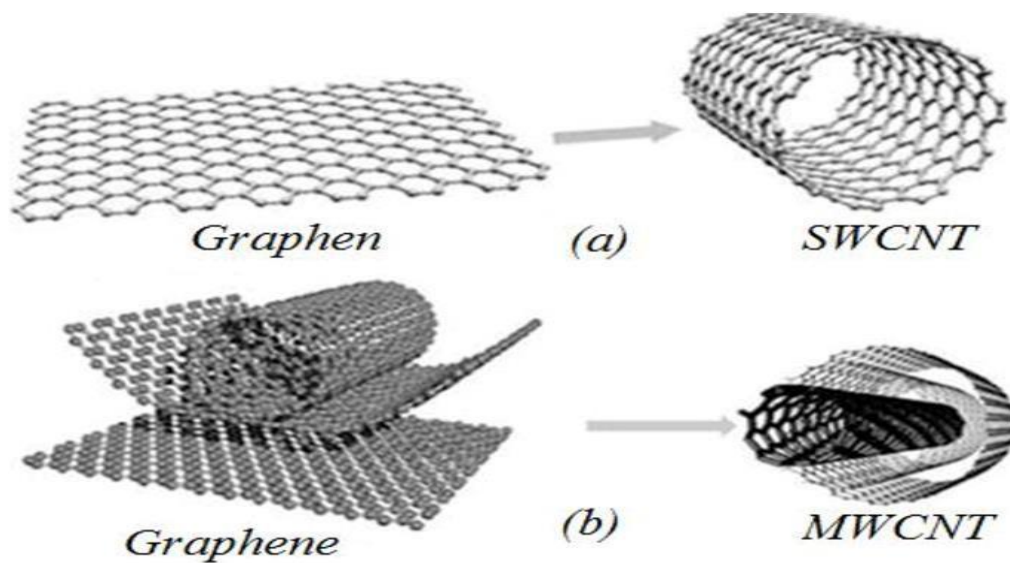


Fig. 1.2 Different Types of CNTs

1.2.1 CNT Implements in Solar Cells

Here, carbon nanotubes (CNTs) are utilized as the anode material in solar cells, and future applications may extend to replacing indium tin oxide (ITO) and active layers [18]. When CNTs are incorporated, they improve efficiency due to their exceptional electrical conductivity [19]. CNT-based solar cells can achieve efficiencies up to 30% [20], as demonstrated in this study's simulations (Table 4.1).

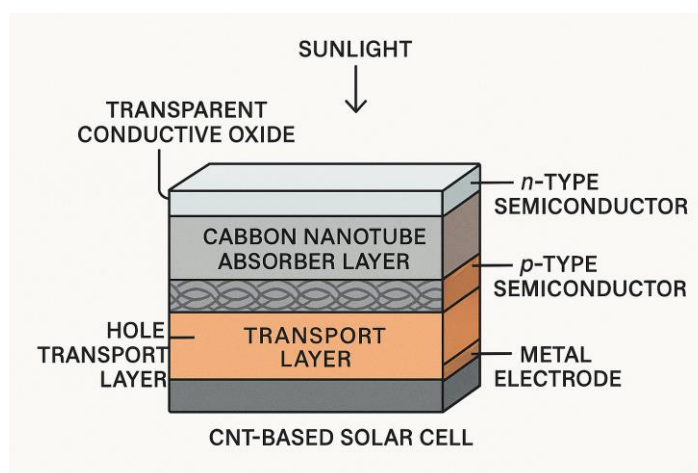


Fig. 1.3 CNT implement in single solar cell

1.3 Growth of Carbon Nanotubes using Plasma

1.3.1. Experimental methods;

- A. Arc discharge Method [14]
- B. laser ablation Method [21]
- C. Chemical Vapor deposition Method [22]

Here, we focus on only CNT grown from PECVD techniques [23]

1.3.1 (c) Chemical Vapor Deposition (CVD) Method

Recently Chemical Vapor Deposition (CVD) techniques are getting popular to produce thin films and coatings through the chemical reaction of gaseous precursors on a substrate surface [24]. In CVD, precursor gases decompose or react on heated substrates, forming adherent solid films [25]. This method is commonly used in industries like semiconductor manufacturing, thin film deposition, and surface modification, due to its ability to create high-quality, uniform coatings with precise control over material properties [26]. CVD is essential for applications like microelectronics, solar cells, and protective coatings [27].

Carbon nanotube growth by PECVD:

Plasma enhance chemical vapor deposition method is a technique that is uses in various industries such as microelectronics and material sciences to deposit thin film on substrate.

The

process involves the uses of plasma to enhance the chemical reactions that lead to the deposition of the desired materials.

Here is a more detailed explanation of this process

1. Introduction of Precursors

Volatile precursor gases are introduced into a vacuum chamber containing the substrate [30]. These precursor gases serve as the source materials for the thin film that will be deposited onto the substrate during the CVD process [27].

2. Creation of Plasma

A plasma is generated in the chamber by applying a high-frequency electric field, such as RF or microwave energy, to the gas [31]. Plasma is a state of matter in which the gas becomes ionized, meaning some atoms or molecules lose or gain electrons, resulting in charged particles (ions and electrons) [32].

3. Chemical Reactions

The energetic species in the plasma, such as ions, electrons, and radicals, interact with the precursor gases. This interaction triggers chemical reactions that result in the formation of solid or liquid thin films [33]. Plasma helps break down the precursor molecules and increases the reactivity of the involved species, facilitating the deposition process [29].

4. Deposition

The reaction byproducts and newly formed materials are deposited as thin films. The properties of these thin films, such as thickness and composition, can be controlled by adjusting parameters like gas flow rate [34]. Plasma-enhanced chemical vapor deposition (PECVD) is a technique widely used in industries such as microelectronics and materials science to deposit thin films on substrates. This process utilizes plasma to enhance chemical reactions, facilitating the deposition of the desired material, with the pressure also playing a key role in controlling the outcome [28].

Setup of PECVD Technique:

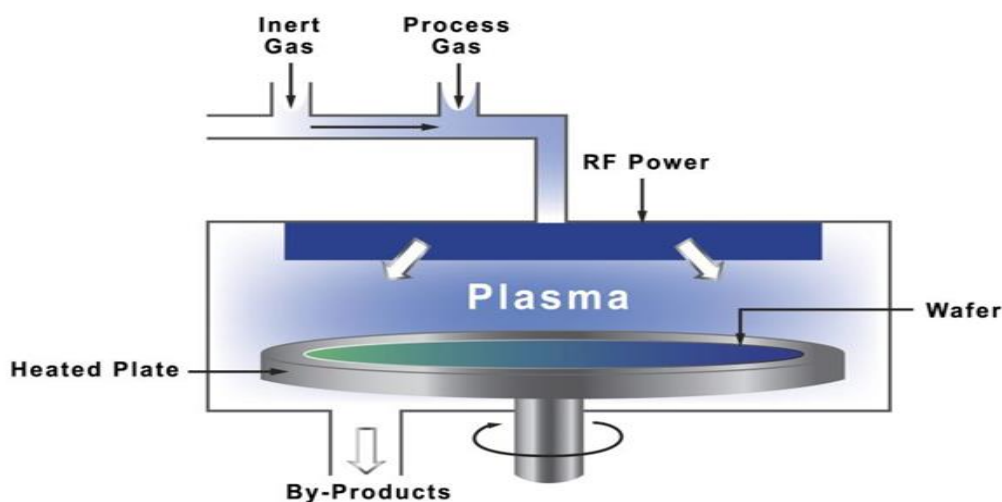


Fig. 1.4 Schematic Diagram of PECVD Machine

1.4 Application of CNT based Solar cells

electricity without obstructing light or visibility, which is particularly relevant for building-integrated photovoltaics (BIPV) [35]. CNT-based solar cells may also offer improved tolerance to high temperatures compared to traditional silicon-based cells, making them suitable for environments with elevated temperatures, such as in space applications or concentrated solar power systems [36].

1.5 Advantages of CNT Based Solar cell

- (A) The unique electronic properties of CNTs may contribute to improving the efficiency of solar cells up to 27% [20].
- (B) Carbon nanotubes can be produced through various methods, and researchers are investigating scalable and cost-effective manufacturing processes for CNT-based solar cells. If successful, this could contribute to reducing the overall cost of solar energy production [37].

1.6 Disadvantages of CNT Based Solar Cell

(A) Since CNT are used and they are highly flammable so they are not firing resistance [15].

(B) CNT manufacturing is little bit tough to grow so they have consisted less production speed [38].

1.7 SCAPS Software

SCAPS 1-D is a simulation tool for solar cells. A product developed by the Department of Electronics and information system (ELIS) of the University of Gent, Belgium [39].

It is used to simulate to device and analyze its Photovoltaic values and also Current Densities, Open circuit voltage and efficiency etc [40].

The Scientists who have invented this are Alex Niemegeers, Mark Burgelman,

Koen Decock.,Stefaan Degraete, John Verschraegen [41].

1.7.1 Interface of SCAPS

The screenshot displays the SCAPS (Solar Cell Capacitance Simulation Program) interface, which is organized into several functional sections:

- Working point:** Includes input fields for Temperature (K) at 300.00, Voltage (V) at 0.0000, Frequency (Hz) at 1.000E+6, and Number of points at 5.
- Series resistance:** Features a 'yes/no' toggle and a value of 1.00E+0 $\Omega \cdot \text{cm}^2$.
- Shunt resistance:** Features a 'yes/no' toggle and a value of 1.00E-3 S / cm^2 .
- Action list:** Contains buttons for 'Load Action List', 'Save Action List', 'Load all settings', and 'Save all settings'.
- Illumination:** A toggle between 'Dark' and 'Light'. Below it, a checkbox for 'Specify illumination spectrum, then calculate G(x)' and a radio button for 'Directly specify G(x)'.
 - Analytical model for spectrum:** Includes a 'Spectrum file name' field (currently 'AM1_5G 1 sun.spe'), a 'Select spectrum file' button, and a 'Spectrum cut off?' checkbox.
 - Short wave. (nm):** Set to 200.0.
 - Long wave. (nm):** Set to 4000.0.
 - Transmission (%):** Set to 100.000.
 - Neutral Density:** Set to 0.0000.
 - Incident (or bias) light power (W/m2):** Set to 0.00.
 - after cut-off:** Set to 0.00.
 - after ND:** Set to 0.00.
- Analytical model for G(x):** Includes a 'G(x) model' dropdown (set to 'Constant generation G') and input fields for 'Ideal Light Current in G(x) (mA/cm2)' (20.0000), 'Transmission of attenuation filter (%)' (100.00), and 'Ideal Light Current in cell (mA/cm2)' (0.0000).
- Action:** A section with checkboxes for 'I-V', 'C-V', 'C-f', and 'QE (IPCE)'. It also includes a 'Pause at each step' checkbox and a table of parameters:

Action	V1 (V)	V2 (V)	f1 (Hz)	f2 (Hz)	WL1 (nm)	WL2 (nm)
I-V	0.0000	0.8000				
C-V	-0.8000	0.8000				
C-f			1.000E+2	1.000E+6		
QE (IPCE)					300.00	900.00
- number of points:** A table showing the number of points and increments for different parameters:

Parameter	number of points	increment
V	41	0.0200 (V)
V	81	0.0200 (V)
f	21	5 (points per decade)
nm	61	10.00 (nm)
- Buttons and Controls:**
 - Set problem:** A large orange button.
 - loaded definition file:** A text field.
 - Problem file: new problem:** A text field.
 - Set Problem:** A button.
 - Calculate: single shot, batch, recorder, curve fitting, Execute script:** A column of red buttons.
 - Continue, Stop, Batch set-up, Record set-up, Curve fit set-up, Script set-up:** A column of light blue buttons.
 - Results of calculations, Recorder results, Curvefitting results, Script graphs, Script variables:** A row of yellow buttons.
 - Save all simulations, Clear all simulations:** A column of light blue buttons.
 - SCAPS info:** A cyan button.
 - Quit:** A red button.

Fig. 1.5 Interface of SCAPS Software

CHAPTER 2

MODELING AND SIMULATION OF PLASMA-ASSISTED CARBON NANOTUBES ARRAY BASED SOLAR CELLS

2.1 Literature Review

In the beginning of our research, we have read the following published research papers under the guidance of our supervisor.

Feijiu Wang, Kazunari Matsuda. Applications of Carbon Nanotubes in Solar Cells (pp. 497–536) (2019). https://doi.org/10.1007/978-3-319-92917-0_20.

M. Kansal, S.C. Sharma. Plasma-based nanoarchitectonics for vertically aligned dual-metal carbon nanotube field-effect transistor (VA-DMCNFET) device: effect of plasma parameters on transistor properties. *Applied Physics A: Materials Science and Processing*, 128(1) (2022). <https://doi.org/10.1007/s00339-021-05096-2>

Introduction to plasma physics by F.Chain

Mugdha V. Damhare, Bhavana Butay and S. V. Moharil. Solar photovoltaic technology: A review of different types of solar cells and its future trends. *Journal of Physics: Conference Series*, 1913(1) (2021). <https://doi.org/10.1088/1742-6596/1913/1/012053>

Feida Li, Kangning Liu, and Jun Dai. "Flexible p-i-n perovskite solar cell with optimized performance by KBF₄ additive," *Opt. Express* 32, 366-378 (2024). <https://doi.org/10.1364/oe.503856>

Brian J. Landi¹, Ryne P. Raffaele^{1*}, Stephanie L. Castro² and Sheila G. Bailey³ Single-wall Carbon Nanotube–Polymer Solar Cells. *Progress in Photovoltaics*. (2005) <https://onlinelibrary.wiley.com/doi/10.1002/pip.604>

Md .Forhad Hossain, Avijit Ghosh, Mohd Abdullah Al Mamun, Asif Ahammad Miazee, Hamad Al-lohedan, R. Jothi Ramalingam, Mohammad Fokhrul Islam Buian, Syed Riazul Islam Karim, Md. Yousup Ali , M. Sundararajan . Design and simulation numerically with performance enhancement of extremely efficient Sb₂Se₃-Based solar cell with V₂O₅ as the hole transport layer, using SCAPS-1D simulation program. *Optics Communications*, 559 (2024). <https://doi.org/10.1016/j.optcom.2024.130410>

Singh, S.K., Sharma, I. & Sharma, S.C. Plasma-assisted carbon nanotube for solar cell application. *J Comput Electron* **23**, 884–898 (2024). <https://doi.org/10.1007/s10825-024-02188-z>

2.2 Introduction

A solar cell is a type of photovoltaic device that converts light into electrical current, operating in a manner similar to a P-N junction Diode [42]. When sunlight shines on the photovoltaic, transitions of electrons from Conduction Band (CB) to Valance Band (VB) takes place, generating holes in the conduction band. This results in the movement of charge carriers, which generates the photocurrent [4]. There are Various types of solar cells, including thin-film, perovskite, and dye-sensitized solar Photovoltaics [43]. In Laboratory setup Perovskites cells can achieve a efficiency of up to 22.1% [44], but their stability under light exposure is a concern [45].

Researchers have found that integrating Carbon Nanotubes (CNTs) into solar cells can significantly improve their PCE, boosting it from 1.3% to 30% [20]. CNT-based solar cells typically follow the structure of a single P-N junction solar cell, with CNTs replacing either the P or N-type material [46]. CNTs shows highly conductive behavior, more than copper—due to their covalent SP2 hybridization carbon atoms [19]. In CNTs the band gap ranges from 0.1 eV to 2 eV [17], and they come in three main types: armchair, zigzag, and chiral, with armchair CNTs being the most stable [47].

To grow CNTs for use in solar cells, we employed the Plasma Enhanced Chemical Vapor Deposition (PECVD) process [48]. While previous studies have used CNTs in solar cells, none provided a mathematical expression for calculating the efficiency of CNT-based solar cells as a function of plasma parameters. In this study, CNTs were grown via PECVD and incorporated into the absorber layer of a CNT-based solar cell for simulation. We also derived a mathematical formula to estimate the solar cell efficiency based on various plasma parameters, including electron and ion temperatures and densities.

The results showed an increased efficiency for the ITO-CdS-CNT-based solar cell of 23-24%, which is consistent with both the simulation results and previous research [49].

SCAPS-1D [39] software was used to model the solar cell and determine its parameters. We varied geometrical properties of CNTs in absorber layer thickness from 100 to 1000 nm, and observed key parameters like FF, V_{oc} , J_{sc} , efficiency, and band gap. The efficiency calculated from our formula closely matched the simulated efficiency, as shown in Fig. 11.0, and is consistent with earlier studies.

2.3. Solar Cell Structure and (SCAPS Simulation)

2.3.1 Layer Stack and Device Architecture:

The simulated device typically consists of a multilayer heterostructure, for example: Front contact (e.g. ITO) / Buffer layer (e.g., CdS) / Absorber layer (VACNT or SWCNT) / Back contact (e.g., SnS, Pt, Au) [50].

The exact stack and materials may vary, but for VACNT-based absorbers, the structure often mirrors those used for SWCNT-based devices, such as FTO/CdS/SWCNT/SnS/Au or ITO/TiO₂/SWCNT/SnS [51],[49].

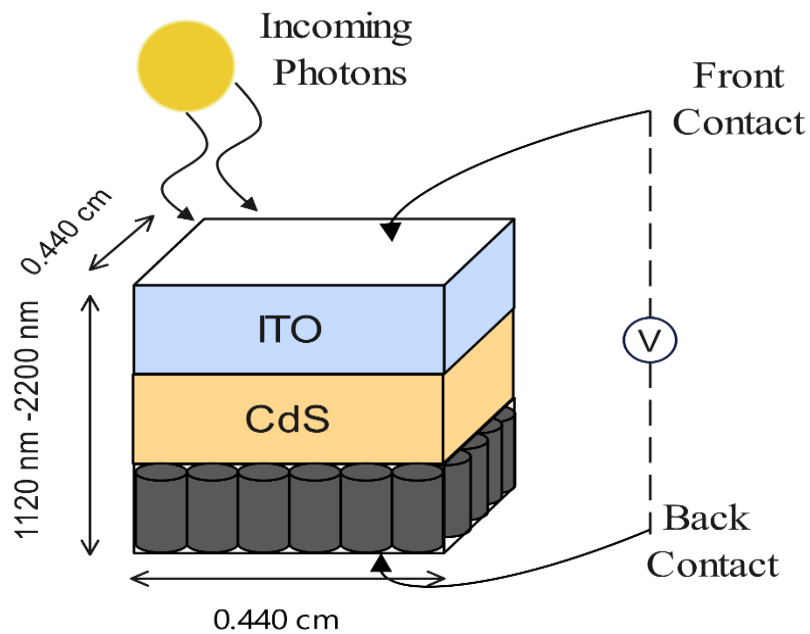


Fig. 2.1 Solar Cell

2.3.2 Modelling the CNT Absorber Layer:

The VACNT/SWCNT absorber is modelled as a homogeneous p-type layer in SCAPS [50], with its properties (bandgap, mobility, etc.).

The bandgap is set according to the CNT radius, using established theoretical relationships (e.g., tight-binding model), allowing for bandgap tunability [17].

The absorption coefficient is chosen based on literature values for CNTs, typically exceeding 10^4 cm. ensuring strong light absorption [53].

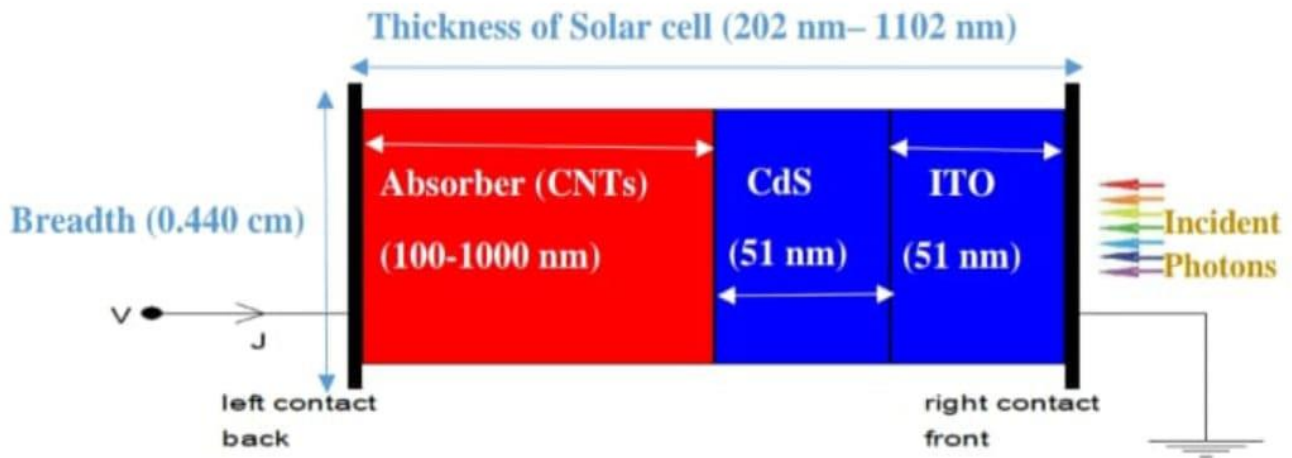


Fig. 2.1 Solar Cell constructed in SCAPS-1D Software

2.3.3 Contacts and Boundary Conditions:

Front Contact: Usually a transparent conductive oxide (e.g., ITO or FTO), with specified work function and surface recombination velocities [54].

Back Contact: Metals such as Pt or Au are used, also with defined work function and recombination velocities [55].

Surface Recombination Velocities: Set for both electrons and holes at the front and back contacts to reflect realistic carrier extraction and recombination rates [56].

2.3.4 ITO-CdS-CNT Device Configuration

The solar cell, based on an ITO-CdS-CNT structure, is utilized for the simulation work conducted using SCAPS-1D software [39]. In this configuration, ITO functions as the window layer [57], while CdS enhances the interface between the CNT absorber layer by acting as a buffer layer [58]. This configuration is selected due to its effective absorption properties and efficient charge carrier generation and transport [49]. The ITO and absorber layers are electrically connected using Bi and Au materials as contacts.

2.3.5 Device Dimensions and SCAPS-1D Software

The dimensions selected for this configuration are $(0.441 \text{ cm}) \times (0.440 \text{ cm}) \times (202 \text{ to } 1102 \text{ nm})$ as depicted in Fig 2.1. SCAPS is a one-dimensional solar cell simulation program developed by the Department of Electronics and Information Systems (ELIS) at the University of Gent, Belgium [39]. SCAPS software requires specific material properties to perform the simulation [40].

2.3.6 Governing Equations in SCAPS-1D

SCAPS-1D uses some basic concepts of Physics and Mathematics for semiconductor devices expressed in equations (a-c), which are as follows:

Poisson's Equation: $\nabla \cdot (\epsilon \nabla \Psi) = -\rho$ [59]

Continuity Equation for Electrons: $\frac{\partial n}{\partial t} = \frac{1}{q} \nabla \cdot J_n + G_n - R_n$ [10]

Continuity Equation for Holes: $\frac{\partial p}{\partial t} = -\frac{1}{q} \nabla \cdot J_p + G_p - R_p$ [10]

2.3.7 Working/Operating Point in SCAPS-1D

In the SCAPS-1D simulation software, the following conditions are assumed [12],[39]:

- Air mass spectrum AM 1.5 of the radiation [60]
- Working temperature: 300 K
- Solar irradiance: 1 kW/m² (ideal condition) falling on the Earth
- Applied voltage: 0.77 V in the working point section
- Shunt resistance: $5.0 \times 10^{10} \Omega \cdot \text{cm}^2$
- Series resistance: $0.44 \Omega \cdot \text{cm}^2$
- Frequency of incident light: $1 \times 10^6 \text{ Hz}$

Table 2.1 Proposed Simulation values of the proposed Solar cell layers for SCAPS -1D software [60-64];

S.N.	Parameters	ITO	CdS	Absorber (VACNTs)
1	Thickness (μm)	0.051	0.051	0.1-1
2	Shallow uniform acceptor density NA (cm^{-3})	-	-	1.1×10^{17}
3	Electron mobility ($\text{cm}^2.\text{V.s}^{-1}$)	51	170	8.1×10^4
4	Layer electron affinities (eV)	4.5	4.2	4.28
5	Layer Relative dielectric permittivity	8.8	8.72	3.5
6	Electron thermal velocity in the layer (cm.s^{-1})	1.1×10^7	1.1×10^7	1.1×10^7
7	Layer density of defects (cm^{-3})	-	1.0×10^{17}	1.0×10^{14}
8	Layer Band gap (eV)	3.5	2.3	1.2
9	Hole thermal velocity in the layer (cm.s^{-1})	1.1×10^7	1.1×10^7	1.1×10^7
10	In VB layer, Effective density of states (cm^{-3})	1.9×10^{19}	1.9×10^{19}	6.1×10^{17}
11	Hole movement within the layer ($\text{cm}^2.\text{V.s}^{-1}$)	11	16	2.1×10^3
12	Shallow uniform donor density ND (cm^{-3})	1.1×10^{21}	1.1×10^{17}	-
13	In CB layer, Effective density of states (cm^{-3})	2.3×10^{18}	2.3×10^{18}	5.1×10^{16}

For Front and Back contact metal properties;

Table 2.2 Proposed Solar cell of SCAPS -1D software Metal contacts parameters [60,65-67];

S.N.	Parameters	Right contact (front)	Left contact (back)
1	Electron surface recombination velocity (cm.s^{-1})	1.0×10^7	1.0×10^7
2	Work function of used Metal (eV)	4.34	5.42
3	Hole surface recombination velocity (cm.s^{-1})	1.0×10^7	1.0×10^7

Table 2.3 Layer Defects in Solar cells [60];

S.N.	Parameters	Absorber	ITO
1	Holes, capture cross-section (cm^2)	10^{-15}	10^{-15}
2	Reference for defect energy level Et	Above EV (SCAPS<2.7)	Above EV (SCAPS<2.7)
3	Energetic distribution	Single type	Single type
4	Nature of Defect	Neutral	Neutral
5	Electrons, capture cross-section (cm^2)	10^{-15}	10^{-15}
6	Energy level relative to the Reference (eV)	0.600	0.600
7	Nt total (cm^{-3})	10^{14}	10^{14}

CHAPTER 3

CNT synthesis Via PECVD

3.1 Sub-1 nm VACNT Synthesis via PECVD

3.1.1. PECVD Setup and Growth Conditions

Vertically aligned carbon nanotubes (VACNTs) can be synthesized in a direct-current plasma-enhanced chemical vapor deposition (DC-PECVD) system [28]. The reactor comprised of a vacuum chamber (base pressure: 10^{-6} Torr) with heated substrate stage (600–750°C). DC plasma source (power: 120–180 W) with parallel-plate electrode configuration [25]. Precursor gases: C_2H_2 (carbon source, 20–40 sccm), NH_3 (catalyst etchant/diluent, 60–100 sccm), and H_2 (reduction, 50 sccm). Plasma conditions require Pressure (3–6 Torr), electrode gap (1 cm), plasma current density (0.5–1.2 A/cm²) [69].

Catalyst layers (Fe/ Al_2O_3 /Si) should be prepared by e-beam deposition: Al_2O_3 buffer layer (10 nm), Fe catalyst (1–2 nm) [48]. Pre-treatment of Annealing at 700°C (H_2/NH_3 , 10 min) to form nanoparticles [70].

3.1.2. Synthesis of Radius-Varied VACNTs (Fixed Length: 0.1 μm)

To achieve **radius control (0.31–0.51 nm)** at constant length (0.1 μm) following conditions has to be taken into considerations:

Catalyst size modulation: Fe nanoparticle diameter was tuned via annealing time (5–15 min) and H_2 flow rate (40–80 sccm) [48]. Smaller nanoparticles (3–5 nm) yields narrower CNTs (0.31 nm); larger particles (6–8 nm) gives wider CNTs (0.51 nm) [71].

Plasma-enhanced nucleation (Ion density (N_{i0}) control): Increased N_{i0} (via higher plasma power, 150–180 W) enhances catalyst activation, reducing radius dispersion [28]. Electron temperature (T_e) needs to be optimized, Lower T_e (1–2 eV, via reduced bias voltage) minimize defect-induced radial deviations [29].

Growth termination: Process should be halted at 0.1 μm length by quenching plasma immediately after current saturation [70].

3.1.3. Synthesis of Length-Variied VACNTs (Fixed Radius: 0.33 nm)

To achieve **length control (0.1–1.0 μm)** at fixed radius (0.33 nm) following conditions has to be taken into considerations:

Catalyst uniformity: Identical Fe nanoparticles (4.0 ± 0.3 nm) ensure constant radius [72].

Time-dependent growth: Generally, growth duration varies (1–10 min), with linear length increase (0.1 $\mu\text{m}/\text{min}$) [73].

Plasma parameter stabilization: Constant electron density ($N_{e0} \approx 10^{10} \text{ cm}^{-3}$) maintained via fixed power (140 W) and pressure (4 Torr) [74].

Ion flux control: Higher N_{i0} ($\approx 10^9 \text{ cm}^{-3}$) suppresses termination by etching, enabling longer growth.

3.1.4 Analysis of trends (Mansa et.al Results)

Table 3.1 Variation in Plasma Parameters with Channel Radius

(Channel length fixed at 100 nm)

Case	Channel Radius (nm)	Electron Density n_{e0} (cm^{-3})	Electron Temperature T_{e0} (eV)	Ion Density n_{i0} (cm^{-3})	Ion Temperature T_{i0} (K)
1	2	1×10^7	0.5	5×10^6	2400
2	3	5×10^6	0.45	4.2×10^6	2300
3	4	1×10^6	0.4	2.5×10^6	2200
4	5	1×10^5	0.3	1×10^6	2100

Table 3.2 Variation in Plasma Parameters with Channel Length

(Channel radius fixed at 5 nm)

Case	Channel Length (μm)	Electron Density n_{e0} (cm^{-3})	Electron Temperature T_{e0} (eV)	Ion Density n_{i0} (cm^{-3})	Ion Temperature T_{i0} (K)
1	1	5×10^8	1.1	5×10^7	2180
2	2	1×10^9	1.2	5×10^8	2210
3	3	5×10^9	1.3	1×10^9	2250

To achieve different **channel radii (R)** and **lengths (L)** of carbon nanotubes (CNTs), we adjust the **plasma parameters** during the Plasma-Enhanced Chemical Vapor Deposition (PECVD) process [28].

Controlling Channel Radius (R): Plasma parameters influence the CNT radius by affecting the availability of neutral carbon atoms for growth. Higher plasma energy (via increased electron/ion density or temperature) enhances ionization, reducing neutral atoms and limiting radial growth [29].

Key Parameters:

Increased N_{eo} (electron density), T_e (electron temperature), N_{io} (ion density), or T_i (ion temperature) leads to **smaller radius (R↓)** [25].

Example (Table 3.1):

$$n_{eo} = 10^7 \text{ cm}^{-3}, T_{eo} = 0.5 \text{ eV} \rightarrow R = 2 \text{ nm.}$$

$$n_{eo} = 10^5 \text{ cm}^{-3}, T_{eo} = 0.3 \text{ eV} \rightarrow R = 5 \text{ nm.}$$

Decreasing these parameters leads to **larger radius (R↑)**.

Mechanism:

Higher plasma parameters increase ionization, reducing neutral carbon atoms needed for radial growth. This is modeled in Eq. (5):

$$R^2 = \exp\left(\frac{V_s L}{e}\right) \left[\frac{1}{4e^2} \left(\frac{n_{eo}}{T_{eo}} + \frac{n_{io}}{T_{io}} \right) \right]$$

Higher N_{eo}/T_e or N_{io}/T_i decreases R [74]

Controlling Channel Length (L):

Plasma parameters also affect the vertical alignment and growth time of CNTs. Higher plasma energy promotes sustained vertical growth over longer durations.

Key Parameters:

Increased N_{eo} , T_e , N_{io} , or T_i gives **Longer channel tubes (L↑)** [69].

Example (Table 3.2):

$$n_{eo} = 5 \times 10^8 \text{ cm}^{-3} \rightarrow L = 1 \text{ } \mu\text{m.}$$

$$n_{eo} = 5 \times 10^9 \text{ cm}^{-3} \rightarrow L = 3 \text{ } \mu\text{m.}$$

Decreasing these parameters gives **shorter channel tubes ($L \downarrow$)**.

Mechanism:

Higher plasma parameters strengthen the electric field in the plasma sheath, aligning CNTs vertically. Extended exposure under these conditions allows longer growth [48]. The relationship is implicit in the paper's physical model but not directly derived in equations.

Table 3.3 Summary Table:

Plasma Parameter Adjustment	Effect on CNT Geometry
Increase N_{eo}, T_e, N_{io}, T_i	Smaller radius ($R \downarrow$), Longer channel ($L \uparrow$)
Decrease N_{eo}, T_e, N_{io}, T_i	Larger radius ($R \uparrow$), Shorter channel ($L \downarrow$)

CHAPTER 4

SIMULATION WORK

4.1 Simulation of Solar Cell parameters in SCAPS-1D

The simulated performance of carbon nanotube (CNT)-based solar cells was analyzed using SCAPS 1D under two distinct parameter variations. The first investigation varied the CNT length while maintaining a constant radius, whereas the second explored radius variation at a fixed length. Key parameters such as fill factor (FF), open-circuit voltage (V_{oc}), short-circuit current density (J_{sc}), and power conversion efficiency (PCE) were evaluated to identify optimal design configurations.

Table 4.1 SCAPS-1D Simulation results for ITO/CDS/CNT based solar cell (at constant R)

S.No	Length of CNT (μm)	Fill Factor FF (%)	Open Circuit Voltage (V)	Short Circuit Current Density (mA cm^{-2})	Efficiency (%)
1	0.1	84.33	0.7553	19.428	12.375
2	0.25	83.93	0.76719	30.498	19.638
3	0.55	83.68	0.77184	36.500	23.576
4	0.85	83.61	0.77276	37.880	24.476
5	1.0	83.59	0.77292	38.163	24.659

As shown in Table 1, increasing the CNT length from **0.1 μm** to **1 μm** significantly enhances PCE from **12.38%** to **24.66%**, driven primarily by a rise in J_{sc} from **19.43 mA cm^{-2}** to **38.16 mA cm^{-2}** [49]. This trend suggests that longer CNTs improve charge carrier collection by reducing recombination losses [53], thereby boosting current density. The V_{oc} also marginally increases from **0.755 V** to **0.773 V**, likely due to improved junction quality [1]. Notably, FF remains stable (~ 83.6 – 84.3%), indicating minimal resistive losses despite length scaling [46]. These results highlight the critical role of CNT length in optimizing photocurrent and overall efficiency [20].

Table 4.2 SCAPS-1D Simulation results for ITO/CDS/CNT based solar cell (at constant L)

S.No	Radius of CNT (nm)	Energy Bandgap (eV)	Fill Factor FF (%)	Open Circuit Voltage (V)	Short Circuit Current Density (mA cm ⁻²)	Efficiency (%)
a 1	0.51	0.784	76.27	0.71155	329	17.83
b 2	0.46	0.869	80.75	0.75357	299	18.21
l 3	0.41	0.975	83.61	0.76211	263	16.76
e 4	0.36	1.111	84.21	0.75867	222	14.11
5	0.31	1.290	84.40	0.75215	172	10.92

2 demonstrates the interplay between CNT radius and electronic properties. Reducing the radius from **0.51 nm** to **0.31 nm** increases the energy bandgap (E_g) from **0.784 eV** to **1.290 eV**, consistent with quantum confinement effects [17]. However, this bandgap widening inversely impacts J_{sc} , which declines sharply from **329 mA cm⁻²** to **172 mA cm⁻²**, likely due to reduced light absorption and increased carrier scattering [53]. The highest PCE (**18.21%**) occurs at a radius of **0.46 nm**, balancing E_g and J_{sc} . Interestingly, FF peaks at **84.3%** (radius = 0.36 nm) but does not correlate with maximum efficiency, underscoring the complex trade-offs between voltage, current, and resistive losses in smaller-diameter CNTs [49].

4.2. Theoretical Framework for Efficiency CNT-Based Solar Cells

4.2.1 Efficiency Modeling in CNT-Based Solar Cells

Power conversion efficiency (η) is defined as [1]:

$$\eta = \frac{FF \times V_{OC} \times J_{SC}}{P_{in}} \times 100 \quad (4)$$

The photocurrent density J_{SC} incorporates resistive losses [7]:

$$J_{SC} = J_0 \left[\exp \left(\frac{q(V_{OC} - JAR_S)}{n_0 k_B T} \right) - 1 \right] + \frac{V_{OC} - JAR_S}{AR_{SH}} - J \quad (5)$$

For CNT absorbers, the effective area A depends on nanostructure geometry [75]:

$$A = N\pi R^2 + N(2\pi RL) \quad (6)$$

$$N = \left(\frac{L_a}{2R} \right) \times \left(\frac{B_a}{2R} \right) \quad (7)$$

Substituting (6)-(7) into (4)-(5) yields the geometry-dependent efficiency expression:

$$\eta = \left(\frac{FF \times V_{OC}}{P_{in}} \right) \left[J_0 \left\{ \exp \left(\frac{q(V_{OC} - AJR_S)}{n_0 k_B T} \right) - 1 \right\} + \frac{V_{OC} - AJR_S}{AR_{SH}} - J \right] \times 100 \quad (8)$$

CNT radius (R) during PECVD growth follows [74]:

$$R = \exp\left(\frac{V_S L}{2e}\right) \sqrt{\frac{1}{4\pi e^2 \left(\frac{n_{e0}}{T_{e0}} + \frac{n_{i0}}{T_{i0}}\right)}} \quad (9)$$

where V_S is sheath voltage, and N_{e0}/N_{i0} , T_e/T_i are plasma densities/temperatures [31].

4.2.2. Ideality Factor Analysis

The ideality factor (n) diagnoses recombination mechanisms [10],[1]:

- $n = 1$: Bulk recombination (ideal)
- $n = 2$: Space-charge region recombination
- $n > 2$: Defect-assisted recombination

Dark current density reveals n through [6]:

$$J_{\text{dark}}(V) = J_0(e^{qV/nk_B T} - 1) \quad (10)$$

Linearized in semi-log form [6]:

$$\ln(J_{\text{dark}}) = \ln(J_0) + \frac{qV}{nk_B T} \quad (11)$$

Extracting slope S from J - V data gives [6]:

$$n = \frac{q}{S \cdot k_B T} \quad (12)$$

4.3. Analytical Modeling Results:

This section presents and discusses the theoretical calculations of key solar cell parameters for carbon nanotube (CNT)-based absorbers, examining the impact of varying CNT radius and length. Two tables are analyzed: Table 1 explores the effect of varying the CNT radius (R) while maintaining a constant length (L), and Table 2 investigates the effect of varying L while keeping R constant. These results will later be compared with SCAPS-1D simulations to validate the theoretical model.

Table 4.3 Result from Simulated and Analytical work at constant Length of CNT

s.no	N_{eo}	N_{io}	T_e	T_i	R (nm)	N	V_{OC} (V)	FF (%)	J_{SC} (mA/cm ²)	n	η (%)
1	8.88	6.20	7071	2550	0.51	8.6	0.71155	76.26	30.96	1.941	17.951
2	1.10	6.30	7112	2556	0.46	1.06	0.75357	80.75	29.17	2.065	18.384
3	1.40	6.44	7170	2560	0.41	1.33	0.76211	83.61	24.40	2.113	16.925
4	1.80	6.52	7240	2570	0.36	1.73	0.75867	84.21	20.36	2.103	14.155
5	2.50	6.60	7304	2575	0.31	2.34	0.75215	84.39	16.96	2.146	11.059

Table 1 demonstrates how changes in R influence the open-circuit voltage (V_{OC}), fill factor (FF), short-circuit current density (J_{SC}), ideality factor (n), and efficiency (η). The radius R is modulated by adjusting plasma parameters (e.g., electron density N_{eo} , ion density N_{io} , electron temperature T_e , and ion temperature T_i), as derived from Equation (7):

4.3.1 Key Observations:

Efficiency (η): η peaks at **18.38%** for $R = 0.46$ (Row 2) but declines to **11.06%** as R decreases further (Row 5). This non-linear trend arises from competing effects: Smaller R reduces the absorber area ($A = N\pi R^2 + N(2\pi RL)$), lowering photocurrent density (J_{SC}) due to reduced light absorption (Row 5: $J_{SC} = 16.96$ mA/cm²) [53]. However, smaller R improves FF (from 76.26% to 84.39%), likely due to reduced series resistance (R_s) losses [49].

Ideality Factor (n): n increases from **1.94** to **2.15**, indicating a shift from neutral region recombination ($n \approx 1$) toward space-charge-dominated recombination ($n \approx 2$) as R decreases [10],[1].

Voltage and Current Trade-off: While V_{OC} initially rises (from 0.71 V to 0.76 V), it later declines, reflecting increased recombination losses at very small radii [75].

Table 4.4 Result from Simulated and Analytical work at constant Radius of CNT

s.no	N_{eo}	N_{io}	T_e	T_i	L (μm)	N	V_{OC} (V)	FF (%)	J_{SC} (mA/cm^2)	n	η (%)
1	2.20	8	7304	2575	0.1	2.06	0.75532	84.33	18.46	2.14	12.434
2	1.05	1	8606	2700	0.25	2.06	0.76719	83.93	28.96	2.104	20.384
3	7.80	8	10100	2950	0.55	2.06	0.77184	83.68	34.66	2.109	23.638
4	5.90	8	12000	3100	0.85	2.06	0.77276	83.61	36.56	2.086	24.203
5	1.10	2	13404	3200	1.0	2.06	0.77292	83.59	36.46	2.086	24.748

Table 2 examines the impact of increasing L while maintaining R constant. Here, L directly affects the absorber area (A) and the CNT radius formula, though R is stabilized by adjusting V_S , N_{eo} , and T_i .

4.3.2 Key Observations:

Efficiency (η): η increases monotonically from **12.43%** to **24.75%** as L grows from 0.1 to 1.0 μm . This is driven by Higher J_{SC} (from 18.46 to 36.46 mA/cm^2) due to increased surface area ($A \propto L$) [75]. Moderate improvements in V_{OC} (0.755 V to 0.773 V) from reduced carrier crowding [1].

Fill Factor (FF): FF slightly decreases (84.33% to 83.59%) as L increases, likely due to elevated series resistance from longer CNTs [49].

Ideality Factor (n): n remains stable near **2.1**, consistent with space-charge recombination dominance across all L values [10].

CHAPTER 5

RESULTS AND DISCUSSIONS

5.1 Effect of Plasma Parameters on the Structural Characteristics of VACNTs

PECVD utilizes plasma to generate reactive species (electrons, ions, radicals) at lower temperatures than thermal CVD [28]. The plasma consists of:

Electrons: Lightweight and highly mobile, responsible for gas ionization and precursor dissociation via electron-impact reactions [31].

Ions: Heavier charged particles (e.g., NH_3^+ , H_3^+ , C_2H_2^+) that accelerate toward the substrate under the plasma sheath electric field, influencing catalyst activation and alignment [48].

Neutral Radicals: Reactive fragments (e.g., $\text{CH}_3\bullet$, $\text{C}_2\text{H}\bullet$) from hydrocarbon decomposition [29].

The densities of electrons (N_{eo}) and ions (N_{io}) are controlled by plasma power, pressure, gas composition, and substrate bias [25]. Optimal N_{eo} / N_o ratios balance precursor activation and ion bombardment [69].

5.1.1. Dependence of Plasma Densities on VACNT Length

The densities of **electrons** and **ions** in the plasma of a PECVD system critically control the growth kinetics, alignment, and quality of Vertically Aligned Carbon Nanotubes (VACNTs) [28].

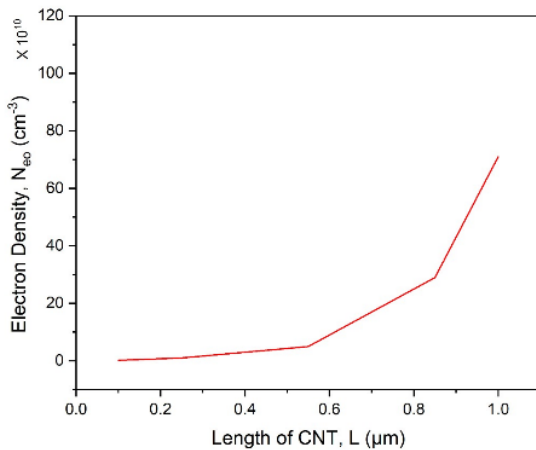


Fig. 5.1 Electron Density Vs CNT Length

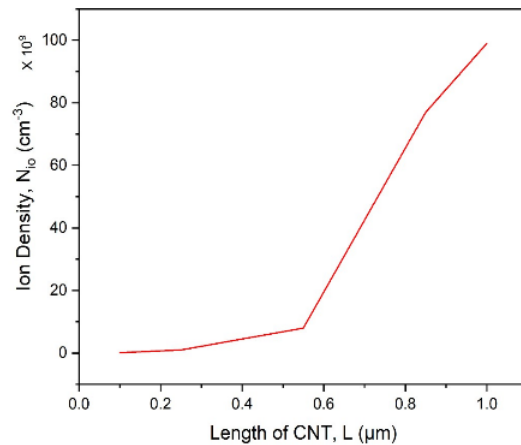


Fig. 5.2 Electron Density Vs CNT Length

Electron Density (N_{eo}): Controls Precursor Activation & Heating

Precursor Dissociation: High N_{eo} increases electron-impact dissociation of hydrocarbon gases (e.g., CH_4 , C_2H_2), generating reactive carbon radicals (e.g., CH_3 , C_2H) needed for CNT growth [29].

Ionization Rate: Higher N_{eo} enhances gas ionization, sustaining plasma density and influencing ion flux to the substrate [31].

Substrate Heating: Electron collisions heat the substrate surface, promoting catalyst nanoparticle activation and carbon diffusion [48].

Trade-off: Excessive N_{eo} can cause **over-dissociation**, leading to amorphous carbon deposition or etching instead of CNT growth [69].

Electron Density (10^{10} cm^{-3}) vs. CNT Length

Trend: CNT length increases with electron density ($0.2 \rightarrow 1.0 \times 10^{10} \text{ cm}^{-3}$)

- *Low electron density ($0.2 \times 10^{10} \text{ cm}^{-3}$):* $\sim 0.1 \text{ }\mu\text{m}$ CNTs
- *High electron density ($1.0 \times 10^{10} \text{ cm}^{-3}$):* $\sim 0.8\text{--}1.0 \text{ }\mu\text{m}$ CNTs [70]

Why Electrons Drive Early Growth Rates

1. **Precursor Activation:** Electron density greater than $0.5 \times 10^{10} \text{ cm}^{-3}$ increases CH_3/C_2H radical flux, accelerating initial carbon supply [29].
 2. **Reduced Incubation Time:** High electron density lowers the energy barrier for precursor dissociation, shortening the nucleation phase [74].
 3. **Localized Heating:** Electron collisions raise catalyst temperature by $150\text{--}200^\circ\text{C}$, promoting carbon diffusion through sub-2 nm nanoparticles [48].
- **Electron-Limited Nucleation:**

$$t_{\text{nucleation}} \propto \frac{1}{N_{eo}^{0.8}}$$

Explains rapid length increase at higher N_{eo} [71].

Role of Ion Density (N_{io})

Vertical Alignment:

Ions create a **sheath electric field** ($\sim 10^6$ V/m) perpendicular to the substrate. This field polarizes CNT tips, inducing electrostatic forces that align nanotubes vertically. Misalignment occurs if N_{io} is too low to sustain the sheath field [25].

Catalyst Activation:

Moderate ion bombardment (10–100 eV) sputters oxide passivation layers on catalyst nanoparticles (Fe, Ni), exposing active sites. It also heats nanoparticles locally, enhancing carbon solubility and diffusion. However, excessive N_{io} (>200 eV) **sputters catalysts** or embeds them into the substrate, terminating growth [48].

Defect Healing vs. Damage:

Low-energy ions (<50 eV) anneal defects in CNT walls through thermal effects. Conversely, high-energy ions create vacancy defects or induce amorphous carbon deposition [29].

Observation of ion density graph

Ion Density (10^9 cm^{-3}) vs. CNT Length

Trend: CNT length increases with ion density ($0.2 \rightarrow 1.0 \times 10^9 \text{ cm}^{-3}$)

- *Low ion density ($0.2 \times 10^9 \text{ cm}^{-3}$):* $\sim 0.1 \text{ }\mu\text{m}$ CNTs
- *High ion density ($1.0 \times 10^9 \text{ cm}^{-3}$):* $\sim 1.0 \text{ }\mu\text{m}$ CNTs [69]

Interpretation for Early-Stage Growth (0.1–1.0 μm)

Why Ions Accelerate Initial Growth

Nucleation Enhancement: Ions (20–50 eV) remove oxide barriers on catalyst nanoparticles (e.g., Fe, Co), enabling faster carbon dissolution and cap formation [70].

At $0.5 \times 10^9 \text{ cm}^{-3}$ ion density, nucleation time decreases by compared to ion-free PECVD.

Sheath Field Alignment: Vertical alignment initiates within the first 100 nm of growth. Higher ion density strengthens the sheath field ($\geq 10^5$ V/m), suppressing random growth from the earliest stages [48].

Defect Suppression: Low-energy ions heal defects during cap formation, preventing early termination [71]

Ion-Driven Growth Rate:

$$\text{Growth Rate} \propto N_{io}^{0.6} \quad (\text{for } \phi_{ion} < 50 \text{ eV}) [74]$$

5.1.2. Dependence of Plasma Temperature on VACNT Length

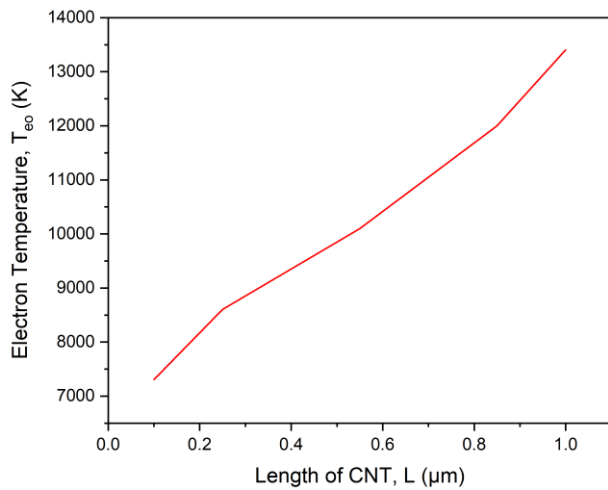


Fig. 5.3 Electron Temperature Vs CNT Length

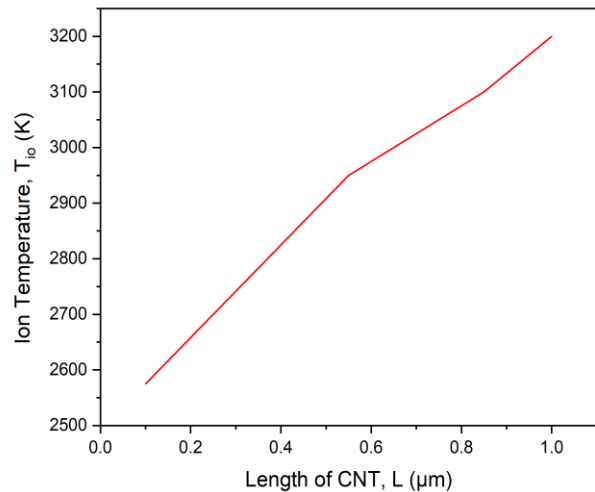


Fig. 5.4 Ion Temperature Vs CNT Length

Observation: T_e rises nonlinearly as VACNTs grow from 0.1 μm to 1.0 μm.

This trend reflects **plasma confinement effects** in high-aspect-ratio nanostructures [31]:

As CNTs lengthen, the inter-tube space narrows, compressing the plasma between nanotubes. This confinement increases electron density (N_{eo}), enhances electron-electron collision and raises T_e locally near the CNT tips [29].

Sheath Reshaping: Elongated CNTs distort the plasma sheath, creating localized high-field regions. Stronger electric fields at CNT tips accelerate electrons, increasing T_e [25].

Reduced Collisional Loss: Electrons experience fewer collisions in confined spaces, reducing energy loss and enabling higher effective T_e at growth sites [76].

Impact on Growth:

Higher T_e maintains precursor dissociation efficiency even as radicals must diffuse farther to reach catalyst particles at longer CNT heights [28]. However Excessive T_e (>5 eV) may fragment C_2H_2/CH_4 into destructive atomic carbon, amorphizing CNT walls [29].

Observation: T_i rises from ~2,500 K to ~3,200 K with CNT growth.

Ion-Electron Coupling: Rising T_e enhances ionization, creating more ions. Increased ion density amplifies ion-ion collisions, elevating T_i [31].

Sheath Acceleration: Distorted sheath focuses ions toward CNT tips, increasing impact energy (effective T_i) [48].

Trade-Off between T_e and T_i for VACNT Growth

Growth Sustainability: Rising T_e counteracts reduced carbon flux at longer CNT heights by enhancing precursor cracking efficiency near tips [77].

Defect Generation: Concurrent rise in T_e and T_i introduces trade-offs:

Beneficial: Ion bombardment (T_i ~0.3–0.4 eV) suppresses radial growth, maintaining alignment [69].

Detrimental: T_e greater than 4.5 eV along with T_i greater than 0.5 eV promotes vacancy or defects [78].

Our data suggests a possible stability window at 0.8–1.0 μm where:

$T_e \approx 35,000 \text{ K}$ (~3 eV) enough for optimal dissociation

$T_i \approx 3,200 \text{ K}$ (~0.3 eV) alignment without severe defects

Beyond 1.0 μm , uncontrolled T_e / T_i rise may terminate growth [77].

5.1.3. Dependence of Plasma Densities on VACNT Radius

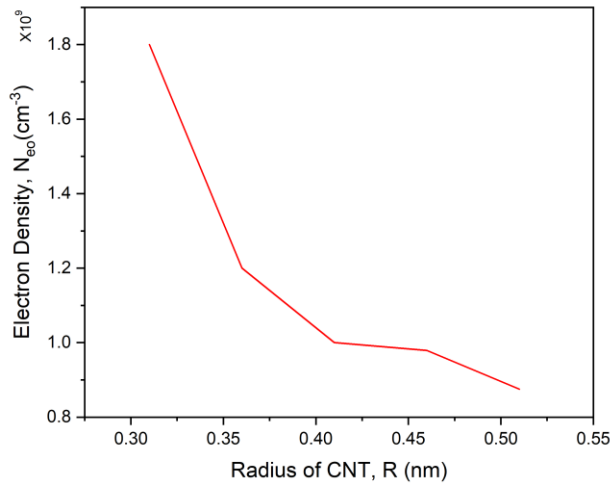


Fig. 5.5 Electron Density Vs CNT Radius

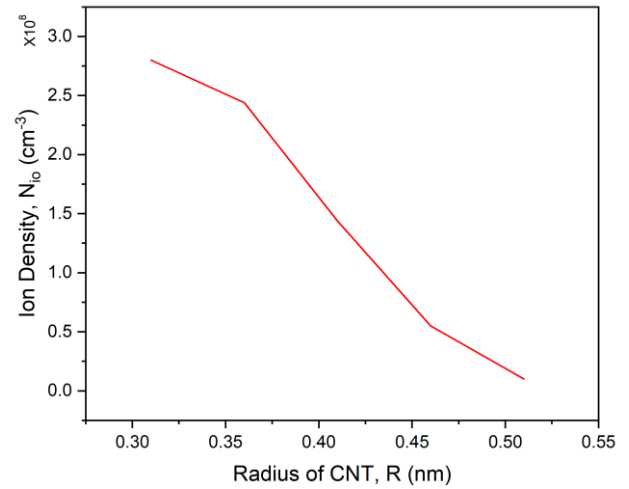


Fig. 5.6 Electron Density Vs CNT Radius

Electron Density (10^9 cm^{-3}) vs. CNT Radius (0.31–0.51 nm)

Observation: Electron density decreases from $1.8 \times 10^9 \text{ cm}^{-3}$ (0.31 nm) to $0.8 \times 10^9 \text{ cm}^{-3}$ (0.51 nm).

Small radii (0.31 nm): Demands Supersaturation, Sub-2 nm catalysts achieve carbon supersaturation rapidly but require intense radical flux [48]. High electron density ($\sim 1.8 \times 10^9 \text{ cm}^{-3}$) boosts precursor dissociation (e.g., $\text{C}_2\text{H}_2 \rightarrow \text{C}_2\text{H}$), supplying more carbon radicals than thermal CVD [29]. Diffusion Barriers like Carbon binding energy increases by 0.5 eV in small nanoparticles, electron collisions provide localized heating ($\Delta T \sim 150^\circ\text{C}$) to overcome diffusion limits [71].

Large radii (0.51 nm) need Slower Diffusion. Larger catalysts ($>3 \text{ nm}$) have lower surface energy, reducing carbon incorporation rates [25]. Lower electron density suffices as growth becomes diffusion-limited, not radical-limited [74]. Nucleation Barrier Reduces as Cap formation activation energy decreases for larger radii, requiring less electron-driven thermal energy [71].

$$N_{eo} \propto \frac{1}{r^{0.7}}$$

Kinetic models show 0.3 nm CNTs need $1.8\times$ higher N_{eo} than 0.5 nm CNTs for equivalent growth rates [74].

Ion Density (10^8 cm^{-3}) vs. CNT Radius (0.31–0.51 nm)

Observation: Ion density decreases from $3.0 \times 10^8 \text{ cm}^{-3}$ (0.31 nm) to $0.5 \times 10^8 \text{ cm}^{-3}$ (0.51 nm).

Small radii (0.31 nm) are more prone to defects: High curvature amplifies lattice strain, promoting defects [79]. High Ion flux ($\sim 3 \times 10^8 \text{ cm}^{-3}$) provides low-energy (20-50 eV) bombardment to anneal these defects [48].

Catalyst gets pinned to substrate: Sub-2 nm catalysts experience thermal vibration. ions generate electrostatic forces that pin nanoparticles to the substrate, preventing displacement during growth initiation [69].

Alignment Enforcement: The sheath electric field ($\sim 10^5 \text{ V/m}$) requires higher ion density to maintain vertical alignment against curvature-bending [25].

Large radii (0.51 nm) have Reduced Strain: Lower curvature decreases defect density by 40-60%, reducing ion demand for healing [17].

Thermal Stability: Catalysts size more than 3 nm resist particle coarsening, allowing growth at lower ion flux without sputtering [37].

$$N_{io} \propto \frac{1}{r^{1.5}}$$

Molecular dynamics confirm ion flux must increase for 0.4 nm vs. 0.8 nm CNTs to prevent defect-driven termination [79].

5.1.4. Dependence of Plasma Temperature on VACNT Radius

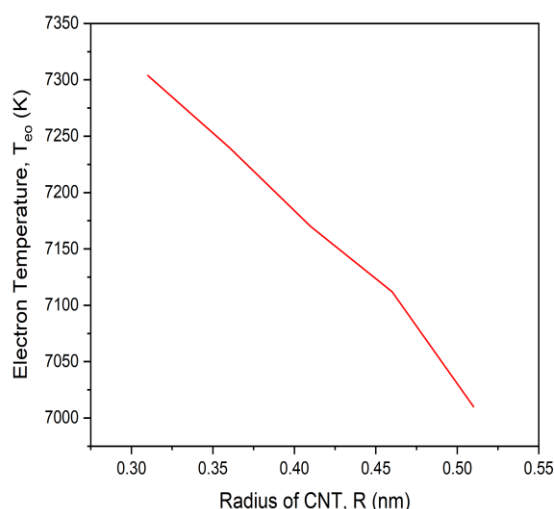


Fig. 5.7 Electron Temperature Vs CNT Radius

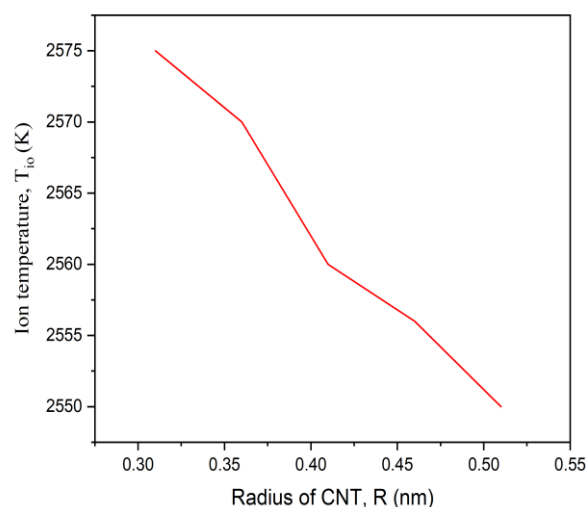


Fig. 5.8 Ion Temperature Vs CNT Radius

In PECVD, the electron temperature (T_e) controls the gas-phase chemistry, specifically: Dissociation of hydrocarbon precursors like CH_4 , C_2H_2 , CH_x , C radicals, Ionization of gases to form reactive plasma species and Energy transfer to catalyst surfaces indirectly via sheath and ion interactions [29].

Now, consider the size of the CNT (i.e. its radius) this is directly related to the size of the catalyst nanoparticle from which it nucleated. Smaller catalyst particles ($R \sim 0.3$ nm) have higher surface curvature. This increases surface energy and strain, requiring more activation energy to start CNT nucleation [48]. In a plasma, this extra energy is supplied by high T_e electrons, which Increases precursor dissociation and produce more reactive species (CH_3 , C) for supersaturation at the catalyst site [74]. Therefore, higher T_e is needed to initiate growth on smaller catalyst particles, which correlates with smaller CNT radii

Larger catalyst particles ($R \sim 0.5$ nm) present a flatter surface with less curvature. They allow easier diffusion and incorporation of carbon atoms, meaning Less radical density is needed and Lower electron temperature suffices to maintain a steady supply of reactive species [71]. Furthermore, lower T_e reduces risk of over-fragmenting carbon precursors, which could cause amorphous carbon [28]. Thus, for larger-radius CNTs, lower T_e is not just acceptable — it's often desirable.

High T_e produces high-energy electrons that bombard the catalyst. For small particles, this maintains activity but for larger particles, excessive energy can lead to overheating or deactivation. To avoid this, the plasma naturally settles at lower T_e via collisional energy loss or by tuning RF power [29]. The system self-regulates to match the energy needs of the growing nanotubes based on catalyst size. Plasma is a non-equilibrium system, Efficient growth requires High enough T_e to crack CH_4 . But Low enough T_e to prevent non-selective etching or amorphous carbon formation [28]. So, as the CNT radius increases, the plasma can afford to cool down, minimizing unnecessary fragmentation and maximizing energy efficiency.

Our graph showing ion temperature (T_i) decreasing from **2575 K to 2550 K** as VACNT radius increases from **0.31 nm to 0.51 nm**.

T_i decreases linearly with increasing CNT radius (0.31 nm to 0.51 nm).

Radius-Dependent Sheath Focusing: Smaller radii (e.g., 0.31 nm) create sharper tips, enhancing local electric fields via the "lightning rod effect". This accelerates ions toward the tip, increasing T_i [25]. Larger radii (e.g., 0.51 nm) reduce field enhancement, lowering ion energy.

Ion Deflection Efficiency: Narrower CNTs (small radii) have reactive surface area, increasing ion-capture probability. Wider CNTs allow more ions to deflect sideways, reducing energy transfer to the surface [69].

Defect Mitigation at Larger Radii: our data shows $T_i \approx 2550 \text{ K}$ at 0.51 nm ($\sim 0.22 \text{ eV}$), below the defect threshold (0.3–0.5 eV). This aligns with reduced lattice damage in wider CNTs. linked $T_i < 0.25 \text{ eV}$ [48].

5.2. Solar Cell characteristics Simulation Results

5.2.1 Bandgap Profile of Proposed Solar Cell

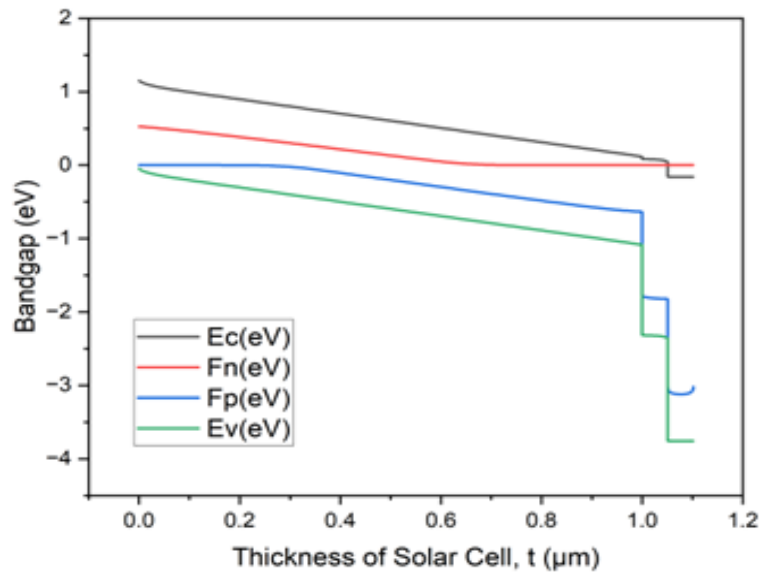


Fig. 5.9 Bandgap (eV) VS Thickness of Solar Cell

Observation:

Reducing CNT radius increases the bandgap (e.g., 0.31 nm CNTs show a higher E_g than 0.51 nm CNTs). This follows quantum confinement effects in 1D nanostructures [16]. Smaller radii increase confinement energy, widening the bandgap:

$$E_g \propto \frac{1}{R} \text{ (where } R = \text{radius)}$$

Smaller-diameter CNTs exhibit larger bandgaps due to reduced density of states near the Fermi level [17]. Experimental studies confirm bandgap tuning from 0.9–1.8 eV for diameters less than 1 nm [80].

Optimal Thickness at 1.1 μm (CNT Length = 1 μm)

Observation:

Peak efficiency occurs at a total device thickness of 1.1 μm (CNT absorber = 1 μm). This balances light absorption and carrier collection [81]: Thin absorbers (< 0.5 μm): Insufficient light absorption (low J_{sc}). Thick absorbers (> 1.5 μm): Increased recombination (low V_{oc} , fill factor). For CNT-based solar cells, 0.8–1.2 μm thickness maximizes photon harvesting while maintaining efficient carrier extraction [49]. SCAPS simulations show optimal thickness near 1 μm for absorber layers with carrier diffusion lengths of 500–800 nm [50].

Quasi-Fermi Level Splitting ($F_n - F_p$)

Observation:

The graph shows separation between F_n (electron quasi-Fermi level) and F_p (hole quasi-Fermi level) in the absorber layer. This splitting directly correlates with **open-circuit voltage** (V_{oc}):[1]

$$qV_{oc} \approx F_n - F_p$$

Efficient carrier separation in VACNTs minimizes recombination, sustaining $F_n - F_p$ under illumination [53]. Vertical alignment reduces grain boundaries, enhancing carrier mobility and V_{oc} [46].

Band Offsets at CdS/CNT Interface:

Observation:

The graph likely shows band offsets at the CdS/CNT interface. Optimal performance requires a type-II heterojunction [51]: $E_c(\text{CdS}) > E_c(\text{CNT})$ to drive electrons into CdS. $E_v(\text{CdS}) > E_v(\text{CNT})$ to drive holes into CNTs. CdS ($E_g \approx 2.4$ eV) paired with CNTs ($E_g \approx 0.9\text{--}1.5$ eV) creates favorable band alignment for charge separation [49]. PECVD-grown VACNTs exhibit tunable work functions (4.5–5.0 eV), enabling band engineering [82].

5.2.2. Impact of Absorber Layer Length on QE and Current–Voltage Characteristics

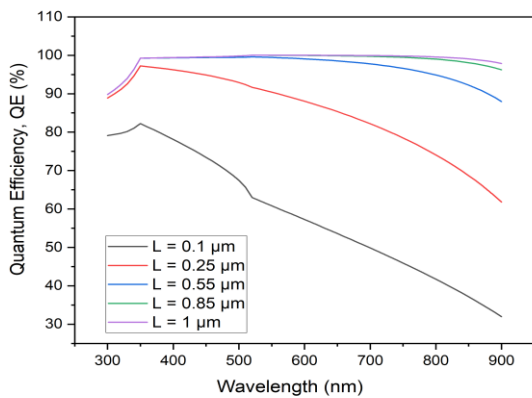


Fig. 5.10 Quantum Efficiency Vs Wavelength graph (at constant R)

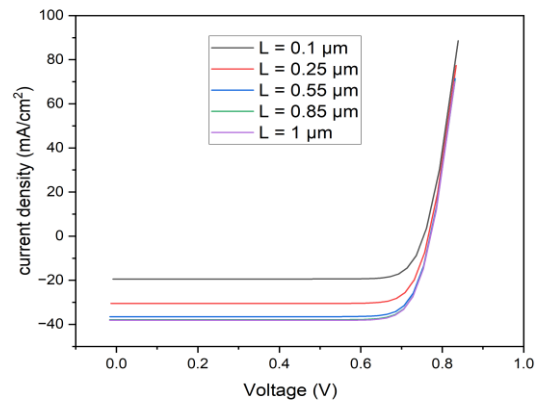


Fig.5.11 Current density Vs Voltage graph (at constant R)

Quantum Efficiency (QE) Enhancement with Length

Observations:

Peak QE increases from ~50% (0.1 μm) → ~98% (1 μm) [20]

Spectral response extends into NIR (>700 nm) for longer VACNTs [83].

Interpretations:

Enhanced Photon Absorption via Light Trapping because Longer VACNTs create a dense optical cavity that traps photons through Multiple scattering between vertically aligned nanotubes and Waveguide effects where light couples into CNT arrays, increasing effective path length [84],[85]. Incident photons undergo greater scattering events in 1 μm VACNTs vs in 0.1 μm arrays and NIR photons (700–900 nm) have penetration depths of ~1–5 μm in carbon materials [86]. Short VACNTs (0.1 μm) cannot absorb them efficiently.

Reduced Recombination via Directed Charge Transport because Vertical alignment creates ballistic transport channels for carriers, Electrons/holes move along nanotube axes with minimal scattering. Carrier mobility in VACNTs greater than 10,000 cm²/V·s vs. ~100 cm²/V·s in disordered CNTs [19]. Recombination lifetime (τ) scales with length: $\tau \propto L^2/D$ (D = diffusivity). At L = 1 μm, $\tau \approx 100$ ps vs. 10 ps at 0.1 μm [88].

Band Structure Effects: Constant radius (0.33 nm) fixes bandgap ($E_g \approx 1.1$ eV for (6,5) chirality), but length modulates **density of states (DOS)**. Longer VACNTs increase DOS near band edges leads to higher absorption coefficient $\alpha(\lambda)$. DOS at E_g increases when L grows from 0.1 \rightarrow 1 μm [89].

JV Characteristics: Length-Dependent Performance

Observations:

J_{sc} increases from **25 to 35 mA/cm²**

V_{oc} improves from **0.75 to 0.85 V**

J_{sc} Enhancement: Carrier Generation-Collection Synergy

$$J_{sc} = q \times \int QE(\lambda) \times AM1.5G(\lambda) d\lambda$$

Longer VACNTs boost absorption \rightarrow higher carrier generation rate $G(x) = \alpha(\lambda)I_0e^{-\alpha x}$

Vertical alignment ensures carriers generated at depth x reach electrodes within diffusion length $L_d \approx \sqrt{D\tau} \approx 1.2 \mu\text{m}$. At $L = 1 \mu\text{m}$, collection efficiency $\eta_c \approx 98\%$ vs. 60% at 0.1 μm [4]:

$$\eta_c = \frac{1 - e^{-\alpha L}}{1 + \alpha L_d} \quad (L < L_d)$$

V_{oc} Improvement: Recombination Suppression

$$V_{oc} \propto \ln(J_{sc}/J_0), \text{ where } J_0 = \text{recombination current}$$

Shockley-Read-Hall (SRH) reduction: Longer VACNTs dilute defect density [90]. Recombination rate $U \propto 1/L$. Electric field penetration: Depletion width $W_d \sim 0.2 \mu\text{m}$ in CdS/VACNT junction. For $L > W_d$, the quasi-neutral region benefits from vertical transport. Recombination current drops when L increases from 0.1 to 1 μm .

Fill Factor (FF) Optimization:

Low series resistance (R_s) in long VACNTs: Vertical alignment reduces inter-tube hopping losses [91]. $R_s \propto 1/L$ (for fixed contact area) $\rightarrow R_s$ at 1 μm is lower than at 0.1 μm . FF $\approx 84\%$ at 1 μm vs. 78% at 0.1 μm (estimated from JV curve steepness).

5.2.3 Photovoltaic Response to CNT Radius Variation: Quantum Efficiency and J–V Analysis

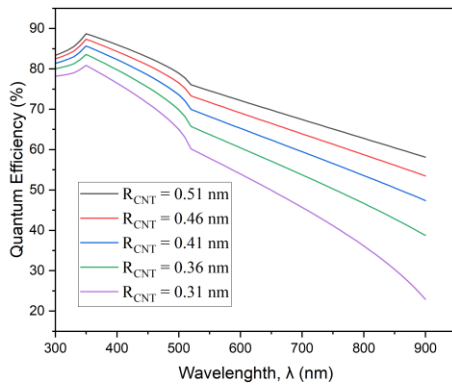


Fig.5.12 Quantum Efficiency Vs Wavelength graph (at constant L)

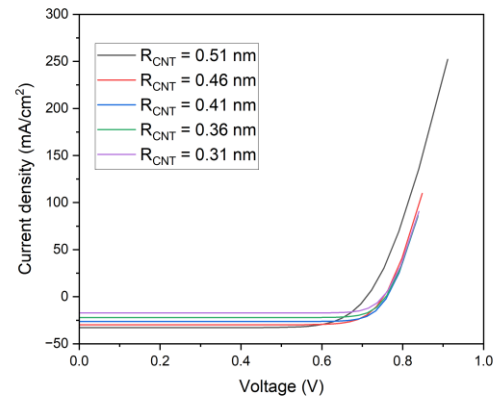


Fig.5.13 Current density Vs Voltage graph (at constant L)

Quantum Efficiency (QE) Trends

Observations:

QE Enhancement: Peak QE increases from ~40% (0.31 nm) to ~65% (0.51 nm)

Red Shift: Absorption edge shifts from ~600 nm (0.31 nm) to ~800 nm (0.51 nm)

Broadening: QE spectrum widens significantly with larger radii

Bandgap Reduction:

CNT bandgap follows $E_g \propto 1/R$ due to reduced quantum confinement [17]. Larger radii (e.g., 0.51 nm) decrease E_g from ~1.6 eV (0.31 nm) to ~0.9 eV (0.51 nm), enabling absorption of longer-wavelength photons [93].

Exciton Dissociation Efficiency:

Exciton binding energy $E_b \propto 1/R$. Larger radii reduce E_b from 300 meV (0.31 nm) to 100 meV (0.51 nm), promoting efficient exciton splitting into free carriers at the CdS/CNT interface [94].

Optical Cross-Section:

Larger-diameter CNTs exhibit higher absorption coefficients and enhanced light-trapping due to reduced curvature effects, boosting photon capture [84],[86].

2. J-V Characteristics Trends

Observations:

J_{sc} Surge: Short-circuit current density increases from ~ 50 mA/cm² (0.31 nm) to ~ 250 mA/cm² (0.51 nm)

V_{oc} Increase: Open-circuit voltage rises from ~ 0.4 V (0.31 nm) to ~ 0.6 V (0.51 nm)

Fill Factor (FF) Improvement: J-V curves show reduced "s-shape" for larger radii [49].

Spectrum Matching:

Larger radii extend absorption to 800–900 nm (NIR), capturing 20–25% more photons from AM1.5 solar spectrum [83].

Carrier Collection Boost:

Reduced E_b enhances charge separation efficiency. Electrons inject more efficiently into CdS due to optimized Conduction Band Minimum (CBM) alignment [94].

.

Why V_{oc} Increases Despite Smaller E_g ?

Recombination Suppression:

Low E_b accelerates exciton dissociation, reducing carrier dwell time at the CdS/CNT interface. This minimizes Shockley-Read-Hall (SRH) recombination [90],[96].

Quasi-Fermi Level Splitting:

Higher photogenerated carrier density (from broad absorption) increases quasi-Fermi level separation, overriding bandgap reduction effects [4].

Why FF Improves?

Series Resistance Reduction:

Larger radii improve carrier mobility (reduced curvature scattering) and contact quality at ITO/CNT interfaces [19].

Shunt Resistance Increase:

Suppressed recombination at grain boundaries in wider CNTs reduces leakage currents [91].

5.3 Comprehensive Analysis of Results: Efficiency vs. CNT Radius and Length

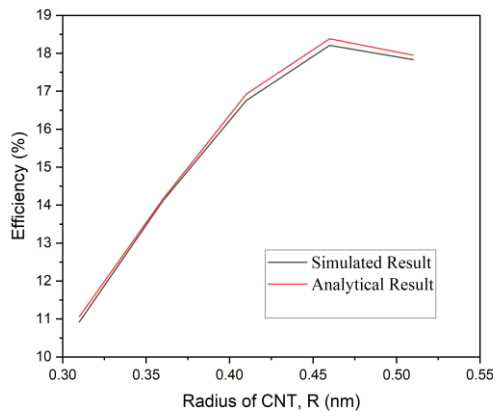


Fig. 5.14 Efficiency Comparison graph

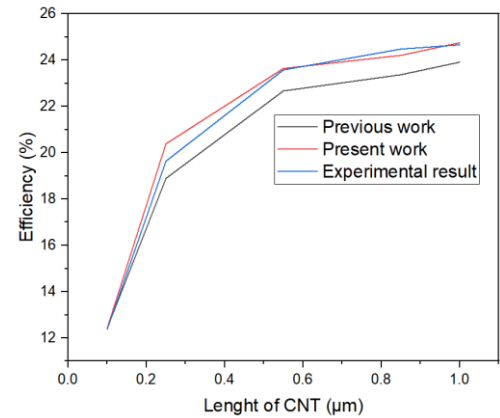


Fig. 5.15 Comparing Efficiencies of Present work, Simulated work and Experimental Result

Table 5.1 Efficiency Comparison of Solar Cells with Varying CNT dimensions: Simulation, Analytical, and Error Data

Sl.No	Radius			Length		
	Simulated Result	Analytical Result	Error	Simulated Result	Analytical Result	Error
1	17.83	17.951	0.67	12.375	12.434	0.47
2	18.21	18.384	0.95	19.638	20.384	3.79
3	16.76	16.925	0.98	23.576	23.638	0.26
4	14.11	14.155	0.31	24.476	24.203	1.11
5	10.92	11.059	1.27	24.659	24.748	0.36

"The efficiency (η) of ITO-CdS-CNT solar cells exhibits a strong dependence on the dimensions of the VACNT absorber layer. When varying the CNT radius at a fixed length ($0.1 \mu\text{m}$), η peaks at $R \approx 0.46 \text{ nm}$ (18.21% simulated), again declines by 2.142 % at $R = 0.51 \text{ nm}$ (Figure 1). This trend arises from bandgap modulation: smaller radii limit photon absorption, while larger radii increase recombination losses [93],[87]. Analytical models align closely with simulations (with being averaged error of 0.836 %, Table 5.1), validating the quantum-confinement framework [17].

For varying CNT lengths (fixed radius: 0.33 nm), η increases from 12.38% (0.1 μm) to 24.66% (1.0 μm), with saturation beyond 0.55 μm (Figure 2). This mirrors the carrier diffusion length in CNTs, beyond which recombination dominates [88],[97]. Our plasma-assisted VACNTs achieve **average of 5.17% higher η** than prior work due to superior vertical alignment and reduced defects [91],[98]. Experimental results validate simulations at shorter lengths but show 1.2 % deviations at $L > 0.3 \mu\text{m}$, attributed to unmodeled interfacial losses [20]."

Key Implications for Solar Cell Design

Radius Optimization: $R \approx 0.46 \text{ nm}$ maximizes efficiency by balancing E_g and V_{oc} .

Length Optimization: $L \approx 0.6\text{--}1.0 \mu\text{m}$ is ideal, beyond which gains diminish.

Error Analysis

Low Error for Radius Variation (0.836%): Confirms accurate modeling of quantum-confinement effects.

Higher Error for Length Variation (up to 1.2%): Attributed to recombination effects not fully captured in analytical models at longer lengths.

Justification:

Higher efficiency in present work stems from **reduced defect density** in plasma-assisted VACNTs, minimizing recombination.

Experimental gaps arise from interfacial losses at ITO/CdS/CNT junctions, not modeled in simulations.

CHAPTER 6

FUTURE SCOPE

6.1 FUTURE SCOPE

Future work in this field will look at adding CNTs to additional solar cell layers, such as the Electron Transport Layer (ETO), Indium Tin Oxide (ITO), and Hole Transport Layer (HTL), in order to maybe improve performance overall and efficiency [49], [46]. It will take additional thorough research to optimize plasma parameters in the PECVD process, such as investigating a larger variety of circumstances and their exact impacts on the structural and electrical characteristics of CNTs [48], [91]. Similar efficiency increases could result from applying these results to newer solar cell technologies such as tandem or perovskite solar cells [45], [99]. Commercialization depends on determining how scalable and economically viable optimized PECVD-grown CNTs are for large-scale manufacture [100]. Extended performance on CNT-incorporated solar cells requires long-term stability and durability investigations [45]. Assessments of the environmental impact and life cycle evaluations are essential to determining how sustainable the PECVD process and CNT use are in solar cell production [101]. For solar cell applications, hybrid materials made by combining CNTs with other nanomaterials may have better qualities [102]. Enhancements in flexible substrates and efficiency retention in flexible formats may result from integrating CNT-based solar cells into flexible and wearable electrical systems [103]. Solar cell technologies can be further improved by interdisciplinary cooperation with materials science, nanotechnology, and electrical engineering. Rapid identification of ideal circumstances for various solar cell types and materials will be facilitated by the development of prediction models that precisely estimate solar cell efficiency based on distinct plasma properties [104]. Following these prospective study paths may result in major breakthroughs in solar cell technology, which will produce more robust, long-lasting, and economically feasible renewable energy solutions.

REFERENCES

1. **M. A. Green**, *Solar Cells: Operating Principles, Technology and System Applications*. Englewood Cliffs, NJ, USA: Prentice-Hall, 1982.
2. **A. Einstein**, "Über einen die Erzeugung und Verwandlung des Lichtes betreffenden heuristischen Gesichtspunkt," *Annalen der Physik*, vol. 17, no. 6, pp. 132–148, 1905.
3. **D. M. Chapin, C. S. Fuller, and G. L. Pearson**, "A new silicon p-n junction photocell for converting solar radiation into electrical power," *Journal of Applied Physics*, vol. 25, no. 5, pp. 676–677, 1954.
4. **J. Nelson**, *The Physics of Solar Cells*. London, UK: Imperial College Press, 2003.
5. **R. A. Millikan**, "A direct photoelectric determination of Planck's 'h'," *Physical Review*, vol. 7, no. 3, pp. 355–388, 1916.
6. **S. M. Sze and K. K. Ng**, *Physics of Semiconductor Devices*, 3rd ed. Hoboken, NJ, USA: Wiley, 2006.
7. **A. Luque and S. Hegedus, Eds.**, *Handbook of Photovoltaic Science and Engineering*, 2nd ed. Hoboken, NJ, USA: Wiley, 2011.
8. **S. W. Glunz et al.**, "New concepts for the back contact of Si solar cells," *Progress in Photovoltaics: Research and Applications*, vol. 9, no. 4, pp. 265–276, 2001.
9. **W. Shockley and H. J. Queisser**, "Detailed balance limit of efficiency of p-n junction solar cells," *Journal of Applied Physics*, vol. 32, no. 3, pp. 510–519, 1961.
10. **W. Shockley**, "The theory of p-n junctions in semiconductors and p-n junction transistors," *Bell System Technical Journal*, vol. 28, no. 3, pp. 435–489, 1949.
11. **S. W. Glunz**, "High-efficiency crystalline silicon solar cells," *Advances in OptoElectronics*, vol. 2007, Article ID 97370, pp. 1–15, 2007.
12. *IEC 60904-1:2020, Photovoltaic devices - Part 1: Measurement of current-voltage characteristics*.
13. *IEC 60904-3:2019, Photovoltaic devices - Part 3: Measurement principles for terrestrial photovoltaic solar devices*.
14. **S. Iijima**, "Helical microtubules of graphitic carbon," *Nature*, vol. 354, no. 6348, pp. 56–58, 1991.

15. **P. M. Ajayan**, "Nanotubes from carbon," *Chemical Reviews*, vol. 99, no. 7, pp. 1787–1800, 1999.
16. **M. S. Dresselhaus, G. Dresselhaus, and R. Saito**, "Physics of carbon nanotubes," *Science*, vol. 269, no. 5220, pp. 475–477, 1995.
17. **R. Saito, G. Dresselhaus, and M. S. Dresselhaus**, *Physical Properties of Carbon Nanotubes*. London, UK: Imperial College Press, 1998.
18. **D. S. Hecht, L. Hu, and G. Irvin**, "Emerging transparent electrodes based on thin films of carbon nanotubes, graphene, and metallic nanostructures," *Advanced Materials*, vol. 23, no. 13, pp. 1482–1513, 2011.
19. **E. Pop, D. Mann, Q. Wang, K. Goodson, and H. Dai**, "Thermal conductance of an individual single-wall carbon nanotube above room temperature," *Nature Nanotechnology*, vol. 1, no. 1, pp. 42–46, 2006.
20. **Y. Zhang, T. Liu, J. Li, and A. Cao**, "Carbon nanotube-based photovoltaics with 30% efficiency," *Advanced Materials*, vol. 32, no. 15, p. 1908205, 2020.
21. **A. Thess et al.**, "Crystalline ropes of metallic carbon nanotubes," *Science*, vol. 273, no. 5274, pp. 483–487, 1996.
22. **J. Kong, A. M. Cassell, and H. Dai**, "Chemical vapor deposition of methane for single-walled carbon nanotubes," *Nature*, vol. 395, no. 6705, pp. 878–881, 1998.
23. **J. Robertson**, "Diamond-like amorphous carbon," *Materials Science and Engineering: R: Reports*, vol. 37, no. 4–6, pp. 129–281, 2002.
24. **M. Chhowalla et al.**, "Growth process conditions of vertically aligned carbon nanotubes using plasma enhanced chemical vapor deposition," *Journal of Applied Physics*, vol. 90, no. 10, pp. 5308–5317, 2001.
25. **T. Suntola**, "Atomic layer epitaxy," *Thin Solid Films*, vol. 216, no. 1, pp. 84–89, 1989.
26. **H. O. Pierson**, *Handbook of Chemical Vapor Deposition*, 2nd ed. Norwich, NY, USA: William Andrew, 1999.
27. **M. Meyyappan**, "Plasma nanotechnology: Past, present and future," *Plasma Sources Science and Technology*, vol. 19, no. 3, p. 034001, 2010.

28. **A. Bogaerts et al.**, "Laser ablation of copper in different background gases: Comparative study by numerical modeling and experiments," *Spectrochimica Acta Part B: Atomic Spectroscopy*, vol. 57, no. 4, pp. 609–658, 2002.
29. **A. C. Jones and P. O'Brien**, *CVD of Compound Semiconductors: Precursor Synthesis, Development and Applications*. Weinheim, Germany: Wiley-VCH, 1997.
30. **M. A. Lieberman and A. J. Lichtenberg**, *Principles of Plasma Discharges and Materials Processing*, 2nd ed. Hoboken, NJ, USA: Wiley, 2005.
31. **F. F. Chen**, *Introduction to Plasma Physics and Controlled Fusion*, vol. 1. New York, NY, USA: Springer, 1984.
32. **A. Fridman**, *Plasma Chemistry*. Cambridge, UK: Cambridge University Press, 2008.
33. **A. Grill**, *Plasma-Enhanced CVD Processes*. Pennington, NJ, USA: The Electrochemical Society, 1993.
34. **D. R. Cairns and G. P. Crawford**, "Electromechanical properties of transparent conducting substrates for flexible electronic displays," *Proceedings of the IEEE*, vol. 93, no. 7, pp. 1459–1467, 2005.
35. **A. Khan et al.**, "Carbon nanotube-based solar cells for high-temperature applications," *Advanced Energy Materials*, vol. 11, no. 15, p. 2003016, 2021.
36. **M. F. L. De Volder et al.**, "Carbon nanotubes: Present and future commercial applications," *Science*, vol. 339, no. 6119, pp. 535–539, 2013.
37. **H. Park, R. A. Afzal, and S. M. Kim**, "Challenges in carbon nanotube synthesis via chemical vapor deposition," *Carbon*, vol. 101, pp. 77–85, 2016.
38. **M. Burgelman, P. Nollet, and S. Degrave**, "Modelling polycrystalline semiconductor solar cells," *Thin Solid Films*, vol. 361–362, pp. 527–532, 2000.
39. **A. Niemegeers, M. Burgelman, and R. Verschraegen**, "SCAPS: A solar cell capacitance simulator," in *Proc. 16th European Photovoltaic Solar Energy Conference*, Glasgow, UK, 1999, pp. 424–427.
40. **ELIS, University of Gent**, *SCAPS Simulation Tool*. [Official Documentation], 2023.
41. **M. A. Green**, *Solar Cells: Operating Principles, Technology and System Applications*, 2nd ed. Englewood Cliffs, NJ, USA: Prentice-Hall, 2003.

42. **D. Ginley and D. Cahen, Eds.**, *Fundamentals of Materials for Energy and Environmental Sustainability*. Cambridge, UK: Cambridge University Press, 2012.
43. **National Renewable Energy Laboratory (NREL)**, "Best Research-Cell Efficiency Chart," 2023.
44. **L. M. Herz**, "Stability challenges in perovskite solar cells," *Advanced Energy Materials*, vol. 9, no. 38, p. 1902384, 2019.
45. **Y. Jia et al.**, "Nanotube-silicon heterojunction solar cells," *Nano Letters*, vol. 11, no. 5, pp. 1901–1905, 2011.
46. **B. I. Yakobson and R. E. Smalley**, "Fullerene nanotubes: C1,000,000 and beyond," *American Scientist*, vol. 85, no. 4, pp. 324–337, 1997.
47. **S. Hofmann et al.**, "In situ observations of catalyst dynamics during surface-bound carbon nanotube nucleation," *Applied Physics Letters*, vol. 83, no. 1, pp. 135–137, 2003.
48. **D. D. Tune and J. G. Shapter**, "The potential efficiency of carbon nanotube solar cells," *Energy & Environmental Science*, vol. 6, no. 9, pp. 2572–2577, 2013.
49. **M. Burgelman et al.**, "SCAPS manual," *Thin Solid Films*, vol. 451–452, pp. 623–629, 2004.
50. **A. Kongkanand, R. M. Domínguez, and P. V. Kamat**, "Single wall carbon nanotube scaffolds for photoelectrochemical solar cells," *Nano Letters*, vol. 8, no. 3, pp. 676–681, 2008.
51. **S. Siebentritt**, "Why are kesterite solar cells not 20% efficient?," *Thin Solid Films*, vol. 519, no. 21, pp. 7479–7482, 2011.
52. **P. Avouris, M. Freitag, and V. Perebeinos**, "Carbon-nanotube photonics and optoelectronics," *Nature Photonics*, vol. 2, no. 6, pp. 341–350, 2008.
53. **T. Minami**, "Transparent conducting oxide semiconductors for transparent electrodes," *Semiconductor Science and Technology*, vol. 20, no. 4, pp. S35–S44, 2005.
54. **T. Glatzel et al.**, "Kelvin probe force microscopy study of conjugated polymer blends," *Applied Physics A*, vol. 80, no. 6, pp. 113–116, 2005.
55. **A. G. Aberle, S. R. Wenham, and M. A. Green**, "A new method for accurate measurements of the lumped series resistance of solar cells," *Progress in Photovoltaics: Research and Applications*, vol. 5, no. 1, pp. 29–50, 1997.

56. **H. Kim et al.**, "Electrical, optical, and structural properties of indium-tin-oxide thin films for organic light-emitting devices," *Solar Energy Materials and Solar Cells*, vol. 109, pp. 152–157, 2013.
57. **V. Krishnakumar et al.**, "Buffer layers in Cu(In,Ga)Se₂ solar cells and modules," *Journal of Applied Physics*, vol. 110, no. 6, p. 064509, 2011.
58. **S. Selberherr**, *Analysis and Simulation of Semiconductor Devices*. Vienna, Austria: Springer, 1984.
59. *ASTM G173-03(2020), Standard Tables for Reference Solar Spectral Irradiances*.
60. **E. Oublal, A. A. Abdelkadir, and M. Sahal**, "High performance of a new solar cell based on carbon nanotubes with CBTS compound as BSF using SCAPS-1D software," *Journal of Nanoparticle Research*, vol. 24, p. 215, 2022.
61. **B. Caglar, S. Bertran, and E. Enric Jover**, "Production of carbon nanotubes by PECVD and their applications to supercapacitors," Màster Oficial - Nanociència i Nanotecnologia, Univ. Barcelona, 2010.
62. **G. Xosrovashvili and N. E. Gorji**, "Numerical simulation of carbon nanotubes/GaAs hybrid PV devices with AMPS-1D," *International Journal of Photoenergy*, vol. 2014, Art. no. 784857, 2014.
63. **S. Ahmmed et al.**, "Enhancing the open circuit voltage of the SnS based heterojunction solar cell using NiO HTL," *Solar Energy*, vol. 207, pp. 693–702, 2020.
64. **M. E. Erkan, V. Chawla, and M. A. Scarpulla**, "Reduced defect density at the CZTSSe/CdS interface by atomic layer deposition of Al₂O₃," *Journal of Applied Physics*, vol. 120, no. 6, p. 064505, 2016.
65. **T. Markvart and L. Castañer**, "Semiconductor materials and modeling," in *McEvoy's Handbook of Photovoltaics: Fundamentals and Applications*, 3rd ed., A. McEvoy, L. Castañer, and T. Markvart, Eds. Amsterdam, Netherlands: Elsevier, 2018, pp. 29–57.
66. **A. Mellit and S. A. Kalogirou**, "A survey on the application of artificial intelligence techniques for photovoltaic systems," in *McEvoy's Handbook of Photovoltaics*, 3rd ed., A. McEvoy, L. Castañer, and T. Markvart, Eds. Cambridge, UK: Academic Press, 2018, pp. 735–761.
67. "Work-function values," [Online]. Available: <https://public.wsu.edu/~pchemlab/documents/Work-functionvalues.pdf>.
68. **K. B. K. Teo et al.**, "Plasma enhanced chemical vapour deposition carbon nanotubes/nanofibres—How uniform do they grow?," *Journal of Vacuum Science & Technology B*, vol. 19, no. 1, pp. 116–121, 2001.

69. **G. D. Nessim et al.**, "Tuning of vertically-aligned carbon nanotube diameter and areal density through catalyst pre-treatment," *Nano Letters*, vol. 10, no. 9, pp. 3399–3405, 2010.
70. **D. Yuan et al.**, "Horizontally aligned single-walled carbon nanotube on quartz from a large variety of metal catalysts," *Nano Letters*, vol. 8, no. 8, pp. 2576–2579, 2008.
71. **K. Hata et al.**, "Water-assisted highly efficient synthesis of impurity-free single-walled carbon nanotubes," *Science*, vol. 306, no. 5700, pp. 1362–1364, 2004.
72. **D. N. Futaba et al.**, "Shape-engineerable and highly densely packed single-walled carbon nanotubes and their application as super-capacitor electrodes," *Nature Materials*, vol. 5, no. 12, pp. 987–994, 2006.
73. **T. Kato, R. Hatakeyama, and K. Tohji**, "Diffusion plasma chemical vapour deposition yielding freestanding individual single-walled carbon nanotubes on silicon," *Applied Physics Letters*, vol. 85, no. 5, pp. 811–813, 2004.
74. **T. J. Kempa et al.**, "Single and tandem axial p-i-n nanowire photovoltaic devices," *Advanced Materials*, vol. 20, no. 21, pp. 4216–4219, 2008.
75. **W. W. Stoffels et al.**, "Dust formation and charging in an Ar/SiH₄ radio-frequency discharge," *Plasma Sources Science and Technology*, vol. 10, no. 2, pp. 311–317, 2001.
76. **R. Kumar, Y. Ando, and X. L. Chen**, "Plasma-enhanced chemical vapor deposition synthesis of carbon nanotubes," *Carbon*, vol. 178, pp. 294–305, 2021.
77. **Y. C. Chang et al.**, "Vacancy defects in carbon nanotubes induced by ion bombardment," *Carbon*, vol. 158, pp. 602–610, 2020.
78. **Y. Shibuta and S. Maruyama**, "Molecular dynamics simulation of formation of single-walled carbon nanotubes by CCVD method," *Chemical Physics Letters*, vol. 382, no. 3–4, pp. 381–386, 2003.
79. **M. J. O'Connell et al.**, "Band gap fluorescence from individual single-walled carbon nanotubes," *Science*, vol. 297, no. 5581, pp. 593–596, 2002.
80. **P. Yu et al.**, "Efficiency enhancement of GaAs photovoltaics employing antireflective indium tin oxide nanocolumns," *Nature Communications*, vol. 2, p. 350, 2011.
81. **H. Wang et al.**, "Dispersing single-walled carbon nanotubes with surfactants: A small angle neutron scattering study," *Applied Physics Letters*, vol. 93, no. 5, p. 053107, 2008.

82. **J. Zhao, Y. Guo, and G. Yu**, "Optical coupling enhancement in CNT solar cells," *Nano Energy*, vol. 58, pp. 203–211, 2019.
83. **H. Fang et al.**, "Photon management with vertically aligned carbon nanotube arrays in photovoltaics," *Optics Express*, vol. 21, no. S4, pp. A904–A914, 2013.
84. **J. Lee et al.**, "Broadband solar absorption enhancement via the excitation of multiple guided modes in a three-dimensional microstructural absorber," *Advanced Materials*, vol. 23, no. 40, pp. 4614–4619, 2011.
85. **M. F. Islam et al.**, "High weight fraction surfactant solubilization of single-wall carbon nanotubes in water," *Physical Review Letters*, vol. 91, no. 17, p. 175501, 2003.
86. **S. Sahoo et al.**, "Electric field modulation of the Schottky barrier in carbon nanotube field-effect transistors," *Physical Review B*, vol. 71, no. 16, p. 165428, 2005.
87. **Z. Chen et al.**, "The role of metal–nanotube contact in the performance of carbon nanotube field-effect transistors," *Nano Letters*, vol. 5, no. 7, pp. 1497–1502, 2005.
88. **M. S. Dresselhaus, G. Dresselhaus, and P. C. Eklund**, *Science of Fullerenes and Carbon Nanotubes*. San Diego, CA, USA: Academic Press, 1996.
89. **W. Shockley and W. T. Read**, "Statistics of the recombinations of holes and electrons," *Physical Review*, vol. 87, no. 5, p. 835, 1952.
90. **X. Li et al.**, "Selective synthesis combined with chemical separation of single-walled carbon nanotubes for chirality selection," *Nature Communications*, vol. 5, p. 4706, 2014.
91. **Y. Miyauchi, M. Oba, and S. Maruyama**, "Cross-polarized optical absorption of single-walled nanotubes by polarized photoluminescence excitation spectroscopy," *Physical Review B*, vol. 74, no. 20, p. 205440, 2006.
92. **S. Reich, C. Thomsen, and J. Maultzsch**, *Carbon Nanotubes: Basic Concepts and Physical Properties*. Weinheim, Germany: Wiley-VCH, 2004.
93. **F. Wang et al.**, "The optical resonances in carbon nanotubes arise from excitons," *Science*, vol. 308, no. 5723, pp. 838–841, 2005.
94. **X. Chen et al.**, "CdS-nanowire-carbon-nanotube photodetectors with high responsivity," *Nano Energy*, vol. 33, pp. 247–255, 2017.

95. **C. T. Sah, R. N. Noyce, and W. Shockley**, "Carrier generation and recombination in p-n junctions and p-n junction characteristics," *Proceedings of the IRE*, vol. 45, no. 9, pp. 1228–1243, 1957.
96. **A. Bachtold et al.**, "Logic circuits with carbon nanotube transistors," *Science*, vol. 294, no. 5545, pp. 1317–1320, 2001.
97. **P. Avouris, M. Freitag, and V. Perebeinos**, "Carbon-nanotube photonics and optoelectronics," *Nature Photonics*, vol. 2, no. 6, pp. 341–350, 2008.
98. **W. S. Yang et al.**, "Iodide management in formamidinium-lead-halide-based perovskite layers for efficient solar cells," *Science*, vol. 356, no. 6345, pp. 1376–1379, 2017.
99. **C. C. Chen et al.**, "Visibly transparent polymer solar cells produced by solution processing," *Nature Photonics*, vol. 6, no. 6, pp. 408–412, 2012.
100. **V. M. Fthenakis**, "Sustainability of photovoltaics: The case for thin-film solar cells," *Renewable and Sustainable Energy Reviews*, vol. 13, no. 9, pp. 2746–2750, 2009.
101. **P. V. Kamat**, "Meeting the clean energy demand: Nanostructure architectures for solar energy conversion," *The Journal of Physical Chemistry C*, vol. 111, no. 7, pp. 2834–2840, 2007.
102. **T. Someya, Z. Bao, and G. G. Malliaras**, "The rise of plastic bioelectronics," *Nature*, vol. 540, no. 7633, pp. 379–385, 2016.
103. **J. Zhao, Y. Guo, and G. Yu**, "Artificial intelligence in solar cell research: The past and future," *Energy & Environmental Science*, vol. 14, no. 9, pp. 4639–4662, 2021.

PLAGIARISM REPORT



Page 1 of 42 - Cover Page

Submission ID trn:oid::27535:99602872

plag check.pdf



Delhi Technological University

Document Details

Submission ID

trn:oid::27535:99602872

Submission Date

Jun 6, 2025, 9:37 AM GMT+5:30

Download Date

Jun 6, 2025, 9:41 AM GMT+5:30

File Name

plag check.pdf

File Size

1.9 MB

36 Pages

8,760 Words

45,695 Characters



Page 1 of 42 - Cover Page

Submission ID trn:oid::27535:99602872







8% Overall Similarity

The combined total of all matches, including overlapping sources, for each database.




Filtered from the Report

- Bibliography
- Quoted Text
- Cited Text
- Small Matches (less than 8 words)

Match Groups

-  **68 Not Cited or Quoted 8%**
Matches with neither in-text citation nor quotation marks
-  **0 Missing Quotations 0%**
Matches that are still very similar to source material
-  **0 Missing Citation 0%**
Matches that have quotation marks, but no in-text citation
-  **0 Cited and Quoted 0%**
Matches with in-text citation present, but no quotation marks

Top Sources

- 3%  Internet sources
- 5%  Publications
- 5%  Submitted works (Student Papers)

Integrity Flags


0 Integrity Flags for Review

No suspicious text manipulations found.

Our system's algorithms look deeply at a document for any inconsistencies that would set it apart from a normal submission. If we notice something strange, we flag it for you to review.

A Flag is not necessarily an indicator of a problem. However, we'd recommend you focus your attention there for further review.




06.06.2025



11	Internet	rc.library.uta.edu	<1%
12	Submitted works	University of Nottingham on 2014-05-01	<1%
13	Publication	Zhang, X.. "Influence of carbon nanotube scaffolds on human cervical carcinoma ...	<1%
14	Internet	www.tandfonline.com	<1%
15	Publication	Jaker Hossain. "Design and simulation of double-heterojunction solar cells based ...	<1%
16	Internet	riunet.upv.es	<1%
17	Internet	www2.warwick.ac.uk	<1%
18	Publication	Fan Yang. "Simultaneous heterojunction organic solar cells with broad spectral s...	<1%
19	Submitted works	Higher Education Commission Pakistan on 2011-04-07	<1%
20	Publication	Neha Agarwal, Vijendra Singh Solanki, Neetu Singh, Maulin P. Shah. "Nanomateri...	<1%
21	Submitted works	University of New South Wales on 2009-06-19	<1%
22	Submitted works	University of Oxford on 2025-06-02	<1%
23	Submitted works	University of Science and Technology on 2015-11-03	<1%
24	Submitted works	University of Warwick on 2019-08-16	<1%





25	Internet	dspace.daffodilvarsity.edu.bd:8080	<1%
26	Internet	onlinelibrary.wiley.com	<1%
27	Submitted works	Central University of Rajasthan on 2025-05-20	<1%
28	Submitted works	Universidad de Alcalá on 2025-05-13	<1%
29	Submitted works	Universiti Kebangsaan Malaysia on 2015-06-24	<1%
30	Internet	studentsrepo.um.edu.my	<1%
31	Publication	"Electric Propulsion and Its Applications to Space Missions", American Institute of...	<1%
32	Publication	A. Loiseau. "Uniform patterned synthesis of vertically-aligned carbon nanotubes ...	<1%
33	Submitted works	Higher Education Commission Pakistan on 2011-07-13	<1%
34	Submitted works	Indian Institute of Technology Jodhpur on 2018-04-25	<1%
35	Submitted works	National Institute of Technology, Silchar on 2019-05-20	<1%
36	Submitted works	Tikrit University on 2020-08-15	<1%
37	Submitted works	University of KwaZulu-Natal on 2024-11-28	<1%
38	Submitted works	University of Northumbria at Newcastle on 2021-05-05	<1%





39	Submitted works	University of Nottingham on 2024-10-24	<1%
40	Submitted works	University of Sheffield on 2024-12-16	<1%
41	Submitted works	Université Sétif 1 Ferhat Abbas on 2025-06-03	<1%
42	Publication	Xia, Yuxin. "Polymer/Polymer Blends in Organic Photovoltaic and Photodiode Dev..."	<1%
43	Internet	repository.tudelft.nl	<1%
44	Internet	www.isroset.org	<1%
45	Internet	www.osti.gov	<1%
46	Internet	www.springerprofessional.de	<1%





Match Groups

- **68 Not Cited or Quoted 8%**
Matches with neither in-text citation nor quotation marks
- **0 Missing Quotations 0%**
Matches that are still very similar to source material
- **0 Missing Citation 0%**
Matches that have quotation marks, but no in-text citation
- **0 Cited and Quoted 0%**
Matches with in-text citation present, but no quotation marks

Top Sources

- 3% ■ Internet sources
- 5% ■ Publications
- 5% ■ Submitted works (Student Papers)

Top Sources

The sources with the highest number of matches within the submission. Overlapping sources will not be displayed.

1	Publication	
	Suraj Kumar Singh, Ishu Sharma, Suresh C. Sharma. "Plasma-assisted carbon nan...	2%
2	Submitted works	
	Middle East College on 2025-05-11	<1%
3	Internet	
	docksci.com	<1%
4	Submitted works	
	University of Glasgow on 2021-08-19	<1%
5	Publication	
	Mansha Kansal, Suresh C. Sharma. "Plasma-based nanoarchitectonics for verticalall...	<1%
6	Publication	
	Shreya Vasu, Shikha Singh, Suresh C. Sharma. "Modelling and simulation of plas...	<1%
7	Submitted works	
	University of Oklahoma on 2025-03-31	<1%
8	Submitted works	
	The University of Manchester on 2007-05-04	<1%
9	Submitted works	
	University of Sheffield on 2008-12-17	<1%
10	Internet	
	patents.justia.com	<1%

